

NEST: Neural Estimation by Sequential Testing

Sjoerd Bruin^{a,*}, Jiří Kosinka^a, Cara Tursun^a

^a*Bernoulli Institute, University of Groningen, Nijenborgh 9, Groningen, 9747AG, The Netherlands*

Abstract

Adaptive psychophysical procedures aim to increase the efficiency and reliability of measurements. With increasing stimulus and experiment complexity in the last decade, estimating multi-dimensional psychometric functions has become a challenging task for adaptive procedures. If the experimenter has limited information about the underlying psychometric function, it is not possible to use parametric techniques developed for the multi-dimensional stimulus space. Although there are non-parametric approaches that use Gaussian process methods and specific hand-crafted acquisition functions, their performance is sensitive to proper selection of the kernel function, which is not always straightforward. In this work, we use a neural network as the psychometric function estimator and introduce a novel acquisition function for stimulus selection. We thoroughly benchmark our technique both using simulations and by conducting psychovisual experiments under realistic conditions. We show that our method outperforms the state of the art without the need to select a kernel function and significantly reduces the experiment duration.

Keywords: psychophysics, adaptive procedures, experimental design, neural networks, active learning

PACS: 0000, 1111

2000 MSC: 0000, 1111

1. Introduction

The relationship between the physical qualities of a stimulus and the perceptual performance can be numerically expressed through psychometric functions (Klein, 2001). Adaptive psychometric procedures are one of the most frequently used methodologies to estimate psychometric functions by determining the sensory thresholds or response characteristics of the *human visual system* (HVS). These procedures adjust the experiment and stimulus parameters in response to the participant’s performance, optimizing the data collection process by choosing the most informative stimulus and experiment parameters to be tested in each trial.

Over the last several decades, a large variety of adaptive psychometric procedures have emerged and become one of the fundamental tools in vision research to study aspects of the HVS such as visual acuity, contrast sensitivity, and color perception (for a review of earlier adaptive psychophysical procedures, please see Treutwein, 1995; Leek, 2001). Despite the success of these procedures, there are still significant challenges that remain to be addressed when the experiment and stimuli are defined by a high-dimensional parameter space. These challenges manifest themselves as slow convergence of the procedure and having an unknown form of the high-dimensional psychometric function. Slow convergence is mainly due to the well-known problem of the so-called “curse of dimensionality”,

which is also observed in regression analysis, and requires a sample selection strategy that aims to improve the information gained from each trial while avoiding redundancy. To this end, Kontsevich and Tyler (1999) developed a variation of the well-known quick estimation by sequential testing (*QUEST*) procedure from Watson and Pelli (1983) called *Psi* that uses entropy minimization to select the next stimulus to test, rather than simply using the mode of the posterior probability distribution. The *Psi* method can also handle the types of stimuli characterized by two-dimensional parameter vectors (Lesmes et al., 2006, 2010; Vul et al., 2010). Watson (2017) developed a framework called *QUEST+* based on the *Psi* method which includes some other capabilities, such as handling an arbitrary number of trial outcomes instead of being limited to binary (e.g., detection/no detection) responses.

Although these methods provide efficient test sample selection in each trial, they require the user to specify the parametric form of the psychometric function. In practice, the parametric form may not be known, especially for complex stimuli and experiments with multiple parameters. Moreover, parametric methods require computation and storage of multidimensional probability distributions, which become intractable as the number of dimensions increases. To address this issue, a class of nonparametric methods based on the *Gaussian process* (GP) (MacKay, 1998) was developed, such as those of Song et al. (2015) and Gardner et al. (2015). GP methods replace the explicit parametric form of the psychometric function with a generic kernel function, which makes them independent

*Corresponding author. Email address: s.bruin@rug.nl

of the number of stimulus and experiment parameters. Samples are usually selected by optimizing an *acquisition function*, which measures the amount of potential improvement in the psychometric function estimation from a newly selected sample (e.g., *Bayesian active learning by variance* (BALV) by Settles (2009), *Bayesian active learning by disagreement* (BALD) by Houthby et al. (2012), and *level set estimation* (LSE) by Gotovos et al. (2013)). Although GP methods do not require the researcher to specify the parametric form of the psychometric function as input, the researcher must still choose an appropriate kernel and acquisition function. Unfortunately, this choice is not trivial and has a significant impact on the accuracy of the estimation of psychometric functions (Owen et al., 2021). As a result, a significant amount of analysis is required to determine the best kernel function and acquisition function depending on the properties of the underlying psychometric function.

In this paper, we introduce a non-parametric procedure called *Neural Estimation by Sequential Testing* (NEST) that uses a neural network-based psychometric function approximator. Similar to GP methods, our approach keeps computational and storage complexity tractable with high-dimensional stimulus and experiment parameters. However, in contrast to GP methods, we show that our method can accurately approximate the psychometric function for many different problem domains **without** the requirement of carefully selecting an appropriate kernel and acquisition function. Furthermore, we show that NEST has an estimation performance that is on par with or better than the best results produced by the set of GP methods previously benchmarked by Owen et al. (2021) and Letham et al. (2022) on a set of synthetic psychometric functions. In addition to simulation-based benchmarks, we validate our method by showing two real use cases, which is estimating the eccentricity-dependent *contrast sensitivity function* (CSF) and the visibility of spatio-temporal *discrete cosine transform* (DCT) bases. We compare our results with two previous studies, Barten (1999) and Tursun and Didyk (2022). In our analysis, we observe that NEST achieves a comparable level of accuracy in estimating psychometric functions with significantly fewer trials. We expect that NEST will allow studying more complex types of stimuli and multi-dimensional psychometric functions in vision research, which was not feasible or convenient with existing adaptive psychometric procedures.

2. Method

The NEST procedure approximates a multi-dimensional psychometric function using a neural network. The network is trained to map the *stimulus space* to the probability of a correct response from a human observer for a visual task, assuming a stationary psychometric function and statistically independent responses. The general workflow of NEST is shown in Figure 1. The NEST method involves training the neural network using the set of all responses

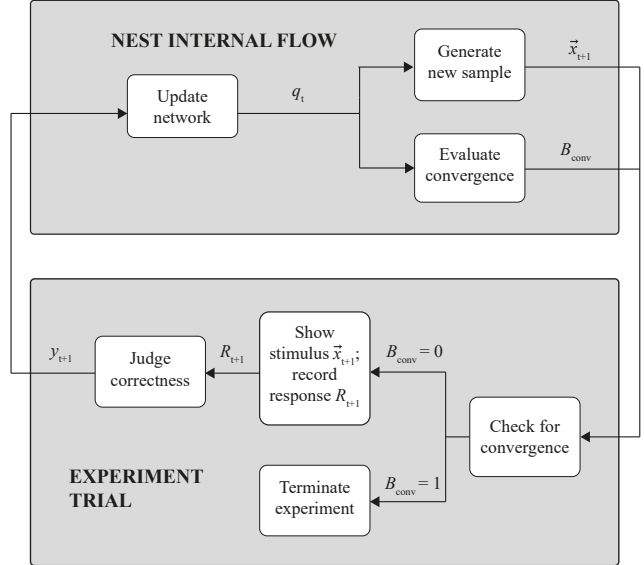


Figure 1: The NEST experiment flow. NEST retrains its network q_t using the updated dataset $D_t = D_{t-1} \cup (\vec{x}_t, y_t)$, then generates a new query \vec{x}_{t+1} by optimizing the acquisition function and evaluates the Fisher convergence criterion to get a binary outcome B_{conv} . The experimenter uses B_{conv} to choose whether to terminate or continue the experiment. If the experiment continues, then a new stimulus is shown based on stimulus parameters \vec{x}_{t+1} , the correctness y_{t+1} of the response is determined, and y_{t+1} is fed back into the NEST algorithm. This process repeats until convergence.

collected after each trial and evaluating whether the experiment has reached convergence for termination of the experiment. Until convergence, the sample for the next trial in the experiment is selected based on an active sampling scheme driven by the *acquisition function*, inspired by Bayesian optimization (Shahriari et al., 2015). In Section 2.1, we describe the detailed architecture of the neural network used to estimate the psychometric function. In Section 2.2, we discuss the sample selection scheme for each trial. Section 2.3 specifies a set of design choices and fixed parameter values in the implementation of the NEST procedure. Finally, in Section 2.4, we explain our novel convergence measure and the experiment termination criterion.

2.1. Neural network architecture

As the psychometric function estimator, our method uses a feedforward artificial neural network, also known as a *multilayer perceptron* (MLP), introduced by Rosenblatt (1961). MLPs are an appropriate choice for the nonparametric estimation of psychometric functions because they are regarded as universal approximators (Hornik et al., 1989). An MLP consists of a sequence of consecutively applied layers of matrix operations defined as

$$q(y|\vec{x}, W) = \sigma_f(W_L \sigma(\dots W_2(\sigma(W_1 \vec{x} + \vec{b}_1) + \vec{b}_2) \dots) + \vec{b}_L), \quad (1)$$

where y represents the probability of a successful trial outcome to a presented stimulus \vec{x} in a detection or discrimination task, L is the total number of network layers, $W = (W_1, \dots, W_L)$ is the sequence of weight matrices with $W_\ell \in \mathbb{R}^{K_{\ell-1} \times K_\ell}$ the ℓ -th weight matrix between the $(\ell-1)$ -th and ℓ -th layer, $\vec{b}_\ell \in \mathbb{R}^{K_\ell}$ is the ℓ -th bias matrix, and $\sigma(\cdot)$ is an operator providing nonlinearity. The network defined by Equation 1 is a general MLP. The final nonlinearity, σ_f , is selected from the family of logistic functions, such that the output of the network defines a proper probability measurement in the range $[0, 1]$. The individual entries of the weight matrices W_ℓ are learned from the stimulus-trial outcome pairs $D = \{(\vec{x}_i, y_i)\}_{i=1}^N$ from the experiment by minimizing the training loss function $L_{\text{train}}(X, Y)$, where $X = (\vec{x}_1, \dots, \vec{x}_N)$ are the input data consisting of stimuli and experiment parameters selected in each trial and $Y = (y_1, \dots, y_N)$ are the corresponding binary training labels that consist of trial outcomes (e.g., detection/no detection in a detection task).

2.2. Sample selection scheme

The problem of developing a quick and efficient testing scheme has been extensively studied as part of the theory of optimal experiments (Fedorov, 2013; MacKay, 1992). Our method shares the same objectives as set by the theory of optimal experiments, which is to select and test the stimulus and experiment parameters that are the most informative about the psychometric function we are trying to estimate. To achieve this goal, we propose a new *acquisition function*, \hat{P}_{acq} , that maps the samples in stimulus space to their intrinsic value for achieving fast convergence. \hat{P}_{acq} is the weighted geometric mean of four components:

$$\hat{P}_{\text{acq}} = (P_{\text{grad}}^a \cdot P_{\text{prox}}^b \cdot P_{\text{unc}}^c \cdot P_{\text{la}}^d)^{\frac{1}{a+b+c+d}}, \quad (2)$$

where P_{grad} favors the selection of samples that maximize the **gradient** of the psychometric function, P_{prox} discourages the **proximity** to the previously selected and queried samples, P_{unc} prioritizes selecting the samples where the model’s **uncertainty** in accurately predicting the outcome of a trial is high, and P_{la} aims to select a sample that has a significant influence on the prediction, based on **lookahead** estimation of retraining the model. The weights a , b , c , and d are optimized for the fastest overall convergence with different types of psychometric functions (Section 4).

During the experiment, the value of \hat{P}_{acq} depends on both the current estimate of the psychometric function and the history of responses accrued in the experiment. Therefore, we compute \hat{P}_{acq} and select the sample that maximizes it in each trial using a gradient descent optimization.

Gradient. The gradient component, P_{grad} , aims to drive the sample selection towards the threshold of the psychometric function, where the gradient magnitude of the estimated function is large. This strategy is also related to

the commonly used heuristics in previous adaptive methods that select samples near the threshold of the psychometric function (Watson and Pelli, 1983; Emerson, 1986; King-Smith et al., 1994). In order to make our computation agnostic to the changes in the maximum gradient magnitude of different functions, we normalize the gradient magnitude as

$$P_{\text{grad}}(\vec{x}) = \frac{|\nabla q(\vec{x})|}{\max_{\vec{z} \in \mathcal{I}} |\nabla q(\vec{z})|}, \quad (3)$$

where \mathcal{I} represents the K -dimensional input space.

Proximity. For non-monotonic psychovisual functions, the gradient term alone tends to oversample around the decision boundary that is discovered at an early stage of the experiment. In order to reduce redundancy and to encourage exploration of the multi-dimensional stimulus and parameter space, the gradient component, P_{prox} , aims to penalize the potential lack of variance in sample selection by assigning a lower intrinsic value to the samples that are in close proximity of prior trials. P_{prox} is inspired from the *kernel density estimation* (KDE) (i.e., *Parzen windows*) method, that maps each new sample \vec{x} to a value that represents its proximity to prior samples $\vec{x}_i \in X$. We use a kernel method instead of other distance measures because it has the advantage of being differentiable in our optimization. We select the Gaussian kernel for our method, which leads to the KDE given by

$$f_{\text{prox}}(\vec{x}, X, h) = \frac{1}{Nh^K (2\pi)^{K/2}} \sum_{\vec{x}_i \in X} e^{-\frac{(\vec{x} - \vec{x}_i)^\top (\vec{x} - \vec{x}_i)}{2h^2}}, \quad (4)$$

where h is the size of the window and corresponds to the standard deviation of the Gaussian kernel. Using Equation 4, we define the gradient component as

$$P_{\text{prox}}(\vec{x}, X, h) = 1 - \frac{f_{\text{prox}}(\vec{x}, X, h)}{\max_{\vec{z} \in \mathcal{I}} f_{\text{prox}}(\vec{z}, X, h)}. \quad (5)$$

Uncertainty. A common strategy used in active learning is *uncertainty sampling*. The fundamental concept of uncertainty sampling is to allow the model to refrain from choosing samples that it is certain about and instead target the areas of the stimuli space that may be perplexing (Settles, 2012; Lewis and Catlett, 1994). A neural network does not provide a built-in way to compute the uncertainty, but Gal and Ghahramani (2016) showed that the well-known dropout technique (Srivastava et al., 2014) against over-fitting can also approximate the network prediction uncertainty.

The *Monte Carlo dropout method* introduced by Gal and Ghahramani (2016) works by replacing the weights W of a network $\hat{q}(y|\vec{x}, W)$ with $\widehat{W} = (\widehat{W}_1, \dots, \widehat{W}_L)$, where

$$\widehat{W}_\ell = \text{diag}\left([z_{\ell,j}]_{j=1}^{K_\ell}\right) W_\ell. \quad (6)$$

With this change, Monte Carlo dropout replaces weights of the network with a function W_ℓ of the random variable $z_{\ell,j}$ with a Bernoulli distribution. Given the output of the dropout neural network $\hat{y}(\vec{x}, \widehat{W}) = \hat{q}(\vec{x}, \widehat{W})$, it is possible to compute the expected output of the network for stimulus \vec{x} as

$$\mathbb{E}_{\vec{x}}[\hat{y}(\vec{x}, \widehat{W})] \approx \frac{1}{M} \sum_{m=1}^M \hat{y}(\vec{x}, \widehat{W}^m), \quad (7)$$

where M is the number of evaluations of the dropout neural network with random sampling of $z_{\ell,j}$. We use the computed variance of the output of the network,

$$\mathbb{V}(\hat{y}(\vec{x}, \widehat{W})) = \mathbb{E}(\hat{y}(\vec{x}, \widehat{W})^2) - \mathbb{E}(\hat{y}(\vec{x}, \widehat{W}))^2, \quad (8)$$

as a measure of the prediction uncertainty for the input sample. Since the output of our neural network is a scalar value, the variance directly translates into the standard deviation $\sigma(\hat{y}(\vec{x}, \widehat{W})) = \sqrt{\mathbb{V}(\hat{y}(\vec{x}, \widehat{W}))}$, and we define our acquisition function term normalized by the maximum value standard deviation takes across the stimulus space as

$$P_{\text{unc}}(\vec{x}) = \frac{\sigma(\hat{y}(\vec{x}, \widehat{W}))}{\max_{\vec{z} \in \mathcal{I}} \sigma(\hat{y}(\vec{z}, \widehat{W}))}. \quad (9)$$

Lookahead. During our initial experiments with the acquisition function components introduced so far, we observed an over-exploration of the stimuli space boundary during sample selection, which was also noted in several previous studies (Siivola et al., 2018; Song et al., 2018; Owen et al., 2021). The model prediction exhibits relatively high uncertainty for the samples along the boundary, which makes them a likely candidate for confidence-based acquisition strategies. Boundary samples are also more likely to be located far from other sample points, and thus favored by proximity-based acquisition schemes, too. The gradient term, meanwhile, does not favor the boundary points, but it does not discourage their selection in general, either. Overall, this trend results in frequently selecting samples from the boundary, which can provide only limited information about the full function domain from the extremes of the stimulus space. We also observed that this issue is exacerbated as the dimensionality of the stimulus space increases.

Letham et al. (2022) showed that a class of acquisition functions called lookahead acquisition functions can perform significantly better in high-dimensional problems by refitting the model on a candidate point and observing the change in the model. For our neural network model, we use the empirical *neural tangent kernel* (NTK) approximation to provide a lookahead mechanism. We follow the definition of Mohamadi et al. (2022) to approximate the behavior of the neural network after retraining with a potential sample from the stimulus space. The lookahead approximation of the network output is given by

$$q_{D^+}(\vec{x}) = q_D(\vec{x}) + \Theta_D(\vec{x}, X^+) \cdot \Theta_D(X^+, X^+)^{-1} \cdot (Y^+ - q_D(X^+)), \quad (10)$$

where \vec{x}' is the potential new sample, D is the training set from the trials conducted so far, $D^+ = D \cup \{(\vec{x}', y')\}$, $X^+ = X \cup \{\vec{x}'\}$, $Y^+ = Y \cup \{y'\}$, and $\Theta_D(a, b)$ is the empirical NTK of two inputs given by

$$\Theta_D(a, b) = \nabla_{\theta} q_D(a) \nabla_{\theta} q_D(b)^T, \quad (11)$$

where θ denotes the parameters of the neural network. Equation 10 allows us to approximate the effect of iteratively training the neural network on the output of the network. In order to maximize the information gained from each trial, we aim to select the sample that maximizes the change in the neural network output.

In order to evaluate the model change, we subsample the stimulus space using *blue noise*, and compute the model outputs for the samples, $\vec{u} \in U$. To consider the worst-case scenario regarding the binary outcomes of the trial, $y' \in \{0, 1\}$, we compute the change in the output of the network for both cases and take the minimum:

$$f_{\text{la}}(\vec{x}, D, U) = \frac{1}{|U|} \min_{y' \in \{0, 1\}} S_{y'} \quad \text{with} \\ S_{y'} = \sum_{\vec{u} \in U} (q_{D \cup \{(\vec{x}, y')\}}(\vec{u}) - q_D(\vec{u}))^2. \quad (12)$$

Based on this definition, the lookahead component $f_{\text{la}}(\vec{x}, D, U)$ is normalized by the maximum value, similar to other components of the acquisition function as

$$P_{\text{la}}(\vec{x}, D, U) = \frac{f_{\text{la}}(\vec{x}, D, U)}{\max_{\vec{z} \in \mathcal{I}} f_{\text{la}}(\vec{z}, D, U)}. \quad (13)$$

2.3. Implementation

Network architecture. As we mentioned earlier in Section 2.1, we use a fully connected MLP network with three hidden layers consisting of 256, 128, and 32 neurons, respectively. In our experiments, we observed that this network size is sufficient even for learning complex and high-dimensional psychophysical functions, which are introduced later in Section 5. Each hidden layer uses *rectified linear unit* (ReLU) activation (Nair and Hinton, 2010).

Initialization. At the beginning of the experiment, we randomly initialize the weights of our network using He initialization (He et al., 2015). We start by performing a random exploration of the stimulus space using Sobol sampling with the probability

$$p_{\text{random}}(t) = \max(p_{\text{base}}, p_0 f^{t-1}), \quad (14)$$

where $p_0 = 0.5$ is the initial random sampling probability, $f = 0.97$ is a factor by which we multiply p_0 after each trial, and t is the current trial number. This formulation gradually shifts from random exploration to the acquisition-function-driven sample selection strategy as the number of trials increases. Eventually, the random sampling probability decreases to the asymptote $p_{\text{base}} = 0.05$. The non-zero asymptote encourages occasional random exploration, even at the later stages of the experiment.

Loss function. We use the *binary cross-entropy* (BCE) loss defined as

$$L_{\text{BCE}}(X, Y) = \frac{1}{N} \sum_{i=1}^N y_i \log q(\vec{x}_i) + (1 - y_i) \log (1 - q(\vec{x}_i)), \quad (15)$$

where $X = (\vec{x}_1, \dots, \vec{x}_N)$ are the input data of selected stimuli, $Y = (y_1, \dots, y_N)$ are the associated binary training labels, and $q(\vec{x})$ is a shorthand for the prediction of the network $q(y|\vec{x}, W, \alpha, \gamma)$. In order to maintain numerical stability, we clamp the value of the logarithmic terms in Equation 15 to the finite range of $[-100, 100]$.

Training. We train the network after each trial of the experiment using the Adam optimizer (Kingma and Ba, 2014) for 100 epochs with a learning rate $\eta_0 = 0.0003$. We additionally apply an exponential learning rate annealing scheme given by

$$\eta(k) = \eta_0 \gamma^k, \quad (16)$$

where k is the epoch number and γ is the decay rate. We set $\gamma = 0.01^{\frac{1}{100}}$ such that the learning rate will decay to $0.01\eta_0$ by the end of the training. In order to avoid overfitting and to increase the stability between trials, we use the *shrink-and-perturb* trick for warm-starting introduced by Ash and Adam (2020).

We apply normalization to balance the scale of different stimulus space dimensions such that we have zero mean and unit variance in each dimension. However, we repeat the normalization only until the 25th trial because we observed that the magnitude of change in mean and variance is negligible after that point.

We set the Parzen window parameter h used in Equation 4 to 0.25. The number of samples M used for Monte Carlo dropout is set to 100. In order to improve the running time, we only evaluate the last dropout layer multiple times (Ma and Kaewell, 2020). For finding the maximum value in Equation 2, we use the *limited-memory Broyden-Fletcher-Goldfarb-Shanno* (LBFGS) optimizer provided by the Scipy library with step size $\epsilon = 10^{-6}$ (Virtanen et al., 2020).

Sample selection. In order to deal with the non-convexity of the acquisition function (Equation 2), we use multiple random initializations. The gradient required for the optimization is computed using automatic differentiation with PyTorch (Paszke et al., 2019).

Scaling the network output. For the final nonlinearity σ_f in Equation 1, we use the Weibull *cumulative distribution function* (CDF) defined as

$$\Psi(x, \rho, T) = 1 - e^{-10^\rho \frac{x-T}{20}}, \quad (17)$$

where T is the *threshold* and ρ is the *slope* of the function (Weibull, 1951). We set $\rho = 1$ and $T = 0$ in our implementation.

In order to scale the output of the network to the range $[0, 1]$ representing a probability, we use

$$q(y|\vec{x}, W, \alpha, \gamma) = \frac{1}{2} (1 + \alpha - \gamma) + \frac{1}{2} (1 - \alpha - \gamma) q(y|\vec{x}, W), \quad (18)$$

where the *lower asymptote* α represents the probability of success for a random response and γ is the *lapse rate*. In our implementation, we selected the Weibull function because it is representative of probability summation among independent detection mechanisms in the HVS (Green and Luce, 1975; Nachmias, 1981); however, the use of other S-shaped functions such as logistic function or the Gaussian integral is also possible.

Regularization. In order to prevent *overfitting*, we apply two types of regularization. The first one is the *dropout* technique introduced by Hinton et al. (2012), whereas the second one is the *input noise injection* introduced by Sitsma and Dow (1991). We set the dropout probability to 0.1, and set $\sigma = 0.01$ for the Gaussian noise while applying input noise injection.

2.4. Termination condition

In order to detect the convergence after each trial $i \in [1, \dots, N]$, we monitor the magnitude of change in the weights of the neural network from the previous trial. More specifically, we compute $\nabla L_{\text{BCE}}(X, Y)$ by following the approach of Liao et al. (2020) and using an approximation of the *Fisher information matrix* (FIM) defined as

$$\tilde{\mathbf{F}}_D = \mathbf{J}_D^T \mathbf{J}_D = (\nabla L_{\text{BCE}}(X, Y))^T (\nabla L_{\text{BCE}}(X, Y)), \quad (19)$$

where \mathbf{J}_D is the Jacobian of the neural network parameters computed based on the dataset D . $\tilde{\mathbf{F}}_D$ is an approximation of the true FIM given by $\mathbf{F}_D = \mathbf{J}_D \mathbf{J}_D^T$, which is prohibitively expensive to compute (Liao et al., 2020). Equation 19 computes the amount of information that the training data contribute to the neural network parameters. We use the cumulative sum of the *Fisher energy* $E(D, K)$ from Liao et al. (2020), which is defined as

$$E(D, K) = \sum_{k=1}^K e(D, k) = \frac{\eta(k)}{NK\eta_0} \sum_{k=1}^K \text{Tr}(\tilde{\mathbf{F}}_D), \quad (20)$$

where K represents the number of training epochs in each trial, $e(D, k)$ is the Fisher energy at epoch k , and $\text{Tr}(\cdot)$ is the trace operator.

Over the course of the experiment, the value of $E(D, K)$ stabilizes when the introduction of new training data no longer provides significant new information to the training. In order to detect convergence, we monitor a 15-trial windowed moving average of the difference between $E(D, K)$ after trial $i - 1$ and after trial i . If the average value in the window drops below a selected threshold value E_{thres} ,

then we assume convergence. A lower E_{thres} represents a more strict stability requirement; however, it will be less likely to detect convergence in the presence of noisy trial outcomes.

We start checking for convergence after at least one negative and one positive sample have been recorded. We provide a detailed analysis of our convergence criterion in the supplementary material.

3. Dataset of synthetic psychometric functions

We use different types of synthetic psychometric functions for learning the weights of the acquisition function (Equation 2) and for a comprehensive performance benchmark of our method with Monte Carlo simulations. Figure 2 shows representative plots of the 2D psychometric functions used in the analysis.

Multidimensional Weibull (WEI1D-4D). The multi-dimensional version of the *Weibull CDF* is given by

$$\Psi(\vec{x}, \vec{\beta}, \vec{T}, \alpha, \gamma) = \alpha + (1 - \gamma - \alpha) \prod_{k=1}^K e^{-10^{\beta_k} \frac{x_k - T_k}{20}}, \quad (21)$$

where $\vec{\beta}$ and \vec{T} are the vectors representing the slope and threshold in each dimension, respectively. The thresholds of the simple multi-dimensional Weibull CDF demarcate a K -dimensional hypercuboid, and transitions along each dimension may have different slopes. This function is a good test case for whether the neural network can model sharp changes in the target function since it needs to approximate the corners of the hypercuboid. We have performed simulations for the *1D Weibull* (WEI1D), *2D Weibull* (WEI2D), *3D Weibull* (WEI3D), and *4D Weibull* (WEI4D) functions.

2D sinusoid (SIN2D). The SIN2D function is a variant of the Weibull CDF for which the threshold value is described by

$$T(x_0, A, f) = A \sin(2\pi f x_0), \quad (22)$$

where x_0 is the first element of two input dimensions, A represents the amplitude, and f represents the frequency of the sinusoidal pattern. We subsequently apply a 1D Weibull CDF using $T(x_0, A, f)$ as the threshold and x_1 as the stimulus dimension. A representative plot of this function is shown in Figure 2.

2D max (MAX2D). The MAX2D function is another variant of the Weibull CDF with a threshold given by

$$T(x_0, c_0, c_f, t) = \max(t, c_0 + c_f x_0), \quad (23)$$

which produces a 2D maximum function with two piecewise linear segments. Watson and Ahumada (2016) proposed that the log-contrast sensitivity of human vision to spatial frequency may be represented with the MAX2D.

2D donut (DN2D). The DN2D function is a variant of the 2D Weibull CDF, whose definition is

$$\Psi(\vec{x}, \vec{\beta}, r_1, r_2, \alpha, \gamma) = \alpha + (1 - \gamma - \alpha) e^{-10^{\beta} \frac{T_d(\vec{x}, r_1, r_2)}{20}}, \quad (24)$$

$$T_d(\vec{x}, r_1, r_2) = \max(\|\vec{x}\|_2 - r_2, r_1 - \|\vec{x}\|_2), \quad (25)$$

where $r_1 < r_2$ are the inner and outer radii of the threshold. As shown in Figure 2, DN2D represents a non-monotonic probability function and therefore tests the capability of modeling a rather complex region (García-Pérez, 2014).

2D novel test (NV2D). This function was introduced by Owen et al. (2021) and defined as

$$\Psi(\vec{x}, \alpha, \gamma) = \alpha - (1 - \alpha - \gamma) \Phi(T_{\text{nt}}(\vec{x}, \alpha, \gamma)), \quad (26)$$

$$T_{\text{nt}}(\vec{x}, \alpha, \gamma) = \frac{4(1 - \alpha)(1 + x_1)}{0.1 + 0.8(0.2x_0 - 1)^2 x_0^2} - 4(1 - 2\alpha), \quad (27)$$

where $\Phi(\cdot)$ is the standard Gaussian CDF.

NV2D represents a general 2D psychometric function and was used by Owen et al. (2021) and Letham et al. (2022) to test the accuracy of their Gaussian process methods, so we include this function as a common testbed.

2D older normal (ON2D). Dubno et al. (2013) defined a number of well-known empirical audiometric functions, one of which is the ON2D function. It has a relatively constant value with only slight upward and downward deviations (Figure 2).

6D Hartmann (HART6). Formulated by Lyu et al. (2021), HART6 is a well-established 6D psychometric function from the family of logistic functions. HART6 allows us to test the capabilities of our method in a higher-dimensional setting. The definition of HART6 is given in Section 1 in suppl. mat.

PS8D. 8D psychometric function (PS8D) is an 8D function, introduced by Letham et al. (2022). We include it in our benchmarks to compare with GP methods. The PS8D function is defined as

$$\Psi(\vec{x}, \alpha, \gamma) = \alpha + (1 - \alpha - \gamma) \Phi\left(\frac{x_1 - c(\vec{x})}{x_5(2 + c(\vec{x}))}\right), \quad (28)$$

where

$$c(\vec{x}) = \left(\frac{x_3}{2} \left(1 - \cos\left(\frac{3}{5}\pi x_2 x_8 + x_7\right)\right) + x_4\right) \cdot \left(2 - x_6 \left(1 + \sin\left(\frac{3}{10}\pi x_2 x_8 + x_7\right)\right)\right) - 1. \quad (29)$$

The input space is $\vec{x} \in [-1, 1]^8$.

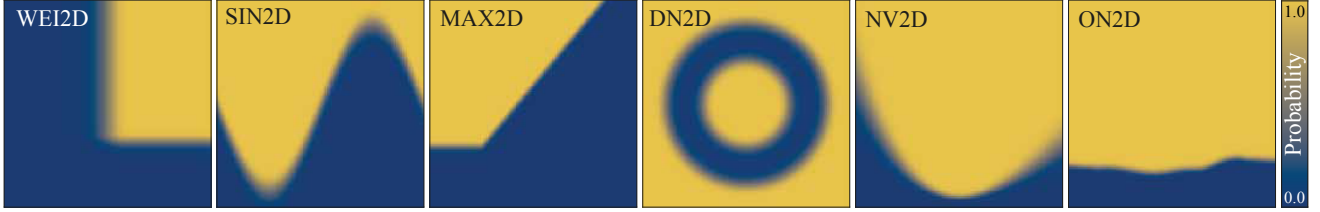


Figure 2: Representative plots of 2D synthetic psychometric functions that we used for calibration and benchmarking. Horizontal and vertical axes represent the input stimulus parameters. We also used higher dimensional psychometric functions that are not visualized here (see Section 3).

4. Learning the acquisition function weights

We optimize the acquisition function weights a , b , c , and d in Equation 2 individually for NV2D, DN2D, SIN2D, WEI4D, and HART6 functions and provide the results in Table 1. We also provide the optimal weights for the set of all psychometric functions, which may be used when the underlying psychometric function type is not known. As expected, the learning and prediction performance improves when we use acquisition function weights specifically optimized for the given psychometric function, but the improvement is limited especially for high-dimensional functions such as HART6. This shows that the acquisition function weights optimized for the combined set of all psychometric functions is still a good choice when the experimenter has no assumptions on the underlying psychometric function.

5. Monte Carlo simulations

For benchmarking, we performed Monte Carlo simulations and also carried out real experiments with multi-dimensional psychometric functions. In this section, we provide our performance metrics (Section 5.1) and then the results of the simulations (Section 5.2).

In our analysis, we use the synthetic psychometric functions introduced in Section 3 as our dataset and perform 100 repetitions for each psychometric function with random selections of its parameters. In addition to our method, we test all of the GP methods from Owen et al. (2021) and the global lookahead methods *expected absolute volume change* (EAVC) and *global mutual information* (GlobalMI) from Letham et al. (2022). Furthermore, we also benchmark the QUEST+ procedure using

WEI1D–WEI4D, SIN2D, and MAX2D psychometric functions. The remaining functions do not have a parametric form that is required by QUEST+. The methods and psychometric functions that we used in our benchmarks are summarized in Table 2.

5.1. Performance metrics

In order to assess the quality of the results, we use two metrics. The first one is the RMSE, which measures the accuracy across the stimulus space and is defined as

$$L_{\text{RMSE}}(\mathbf{Y}_{\text{true}}, \mathbf{X}_{\text{test}}) = \sqrt{\frac{1}{N} \sum_{i=1}^N (y_i - \Psi(\vec{x}_i))^2}, \quad (30)$$

where $\mathbf{Y}_{\text{true}} = (y_1, \dots, y_N)$ and $\mathbf{X}_{\text{test}} = (\vec{x}_1, \dots, \vec{x}_N)$.

The second metric is the *Brier score* developed by Brier (1950) and also used by Letham et al. (2022), defined as

$$L_{\text{Brier}}(\mathbf{Y}_{\text{true}}, \mathbf{X}_{\text{test}}, \mu^*) = \frac{1}{N} \sum_{i=1}^N (o_i - P(\Psi(\vec{x}_i) \geq \mu^*))^2, \quad (31)$$

where $o_i = (y_i \geq \mu^*) \in \{0, 1\}$ is a binary variable that indicates whether the true label y_i is larger than the target

Table 2: An overview of benchmarks for tested methods.

Function	QUEST+	Gaussian Processes	NEST
WEI1D-WEI4D	✓	✓	✓
SIN2D	✓	✓	✓
MAX2D	✓	✓	✓
DN2D	×	✓	✓
NV2D	×	✓	✓
ON2D	×	✓	✓
HART6	×	✓	✓
PS8D	×	✓	✓

Table 1: Optimal parameter settings for individual functions and for all functions combined. The last column shows the percentage improvement in performance when using the optimal acquisition parameter values instead of the values from the combined optimization.

Function	a	b	c	d	AUC _{func}	AUC _{comb}	ΔError
NV2D	4.6	2.6	1.4	3.6	22.60 ± 0.48	25.67 ± 0.28	13.58%
DN2D	8.6	16.0	8.0	7.6	40.51 ± 1.07	47.71 ± 0.87	17.78%
SIN2D	2.8	8.0	3.4	6.0	56.80 ± 0.87	58.84 ± 0.42	3.59%
WEI4D	3.6	15.4	6.6	0.6	41.56 ± 0.82	45.28 ± 0.36	8.97%
HART6	0.4	6.0	7.0	7.2	247.77 ± 1.44	255.17 ± 1.74	2.98%
Combined	0.8	10.6	6.0	4.0	–	–	–

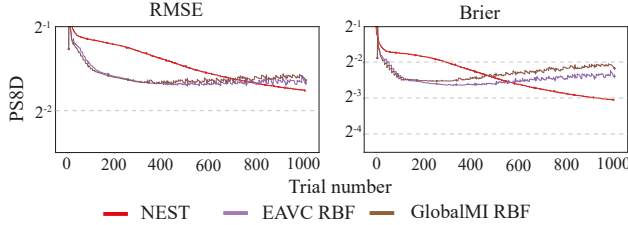


Figure 3: The results for the PS8D function for NEST, and the EAVC and GlobalMI GP methods. Although AUC is higher for NEST, it can achieve better performance scores towards the end of the simulation.

probability μ^* , and $P(\Psi(\vec{x}_i) \geq \mu^*)$ denotes the likelihood that the outcome of the approximated psychometric function is higher than μ^* . We set $\mu^* = \frac{1+\alpha}{2}$, where α is the lower asymptote of the simulation experiment (Equation 18). GP methods automatically encode such a probability distribution over the outcome. For NEST, we use the variance computed using Equation 8 to model a Gaussian distribution and determine the required likelihood. Different from RMSE, which measures only the accuracy, the Brier score takes into account both the accuracy and uncertainty in the estimation by penalizing high confidence in incorrect threshold placement and rewarding high confidence in correct threshold placement. We classify the test samples either as supra- or sub-threshold stimuli and use this binary target to compute the Brier score.

5.2. Results

We benchmark our method, QUEST+, and GP methods using the RMSE and Brier scores for all of the synthetic psychometric functions listed in Table 2. Due to limited space, we provide results only for NV2D, WEI4D, HART6, and PS8D in Table 3. For the remaining psychometric functions, please refer to the supplementary material. We consider the performance across all trials using the *area under curve* (AUC) for the two metrics. The table

shows scores of the best method and the methods whose performance scores do not have a statistically significant difference from the best method (Games and Howell (1976) post-hoc test) in bold typeface.

The LSE GP methods perform poorly in the RMSE error metric but very well in the Brier score since the latter score focuses on threshold accuracy above overall slope accuracy. Despite this, NEST matches the Brier score of the LSE methods in WEI4D and outperforms it in NV2D and HART6. NEST also outperforms the lookahead functions EAVC and GlobalMI in NV2D, WEI4D, and HART6. On the PS8D function, NEST performs slightly below the GlobalMI and EAVC methods. Upon further investigation, we observed that although GlobalMI and EAVC achieve a fast decrease in RMSE and the Brier score at the beginning of the experiment, NEST achieves lower prediction error at the end of the experiment (Figure 3). Overall, NEST either outperforms the GP methods for most tested functions or it is on par with them. QUEST+ performs the best on parametric 1D and 2D functions, but NEST outperforms QUEST+ on higher-dimensional functions like WEI4D.

The kernel function in GP methods should be selected according to the underlying psychometric function type for optimal performance. In Figure 4, stimulus selection and estimation of the NV2D psychometric function is shown for different numbers of trials for one experiment run. In the same figure, we also compare our method with the GP method, using the BALD acquisition function and the linear-additive kernel function defined in Owen et al. (2021). Our approach surpasses GP methods by being more flexible in modeling various psychometric functions, eliminating the need for kernel selection.

6. Validation with psychovisual experiments

We further benchmarked our method by conducting two psychovisual experiments. The first experiment (Sec-

Table 3: The mean *area under curve* (AUC) \pm standard error of the *root mean-squared error* (RMSE) and Brier metrics for the NV2D, WEI4D, HART6, and PS8D functions. The best method(s) for each metric are shown in bold typeface. Our method performs better ($p < 0.03$, Games-Howell test) than the other methods on the NV2D, WEI4D, and HART6 functions. For PS8D, our method has slightly higher AUC, but it achieves the best score for both error metrics at the end of the experiment (see Figure 3 for details). The psychometric functions marked as N/A are not tested with QUEST+ due to the lack of a parametric form (Section 5).

Method	NV2D		WEI4D		HART6		PS8D	
	AUC _{RMSE}	AUC _{Brier}	AUC _{RMSE}	AUC _{Brier}	AUC _{RMSE}	AUC _{Brier}	AUC _{RMSE}	AUC _{Brier}
NEST (ours)	22.69 \pm 0.30	6.03 \pm 0.15	44.04 \pm 0.84	8.25 \pm 0.38	246.52 \pm 2.64	108.75 \pm 2.19	371.39 \pm 0.97	204.77 \pm 1.12
QUEST+	N/A	N/A	110.74 \pm 3.72	N/A	N/A	N/A	N/A	N/A
BALD RBF	28.30 \pm 0.18	11.27 \pm 0.14	78.26 \pm 0.27	19.05 \pm 0.18	287.09 \pm 1.13	307.12 \pm 5.16	375.23 \pm 2.20	291.06 \pm 2.39
BALD mon.-RBF	27.78 \pm 0.19	13.08 \pm 0.17	77.01 \pm 0.35	23.81 \pm 0.23	288.47 \pm 3.25	307.05 \pm 8.81	403.35 \pm 2.19	314.91 \pm 2.17
BALD lin.-add.	35.78 \pm 0.24	17.36 \pm 0.25	106.62 \pm 0.62	23.80 \pm 0.06	342.06 \pm 0.80	360.31 \pm 4.30	394.67 \pm 1.10	282.80 \pm 1.42
BALV RBF	27.05 \pm 0.17	10.45 \pm 0.14	100.63 \pm 0.34	24.61 \pm 0.29	287.18 \pm 1.34	280.11 \pm 27.98	367.21 \pm 4.08	282.56 \pm 2.08
BALV mon.-RBF	26.05 \pm 0.17	12.12 \pm 0.15	58.06 \pm 0.85	10.60 \pm 0.30	284.36 \pm 1.74	281.93 \pm 8.21	397.58 \pm 2.06	308.84 \pm 2.32
BALV lin.-add.	40.70 \pm 0.24	19.31 \pm 0.28	130.00 \pm 0.74	39.19 \pm 0.22	329.77 \pm 1.21	347.69 \pm 4.03	396.92 \pm 1.55	286.47 \pm 1.58
LSE RBF	37.68 \pm 0.23	8.35 \pm 0.07	74.24 \pm 0.37	7.39 \pm 0.07	342.44 \pm 1.37	256.03 \pm 4.48	406.67 \pm 2.75	244.55 \pm 3.51
LSE mon.-RBF	40.84 \pm 0.22	8.33 \pm 0.09	119.14 \pm 3.57	28.07 \pm 1.19	335.37 \pm 2.36	266.34 \pm 19.77	407.75 \pm 3.50	242.43 \pm 4.99
LSE lin.-add.	51.06 \pm 0.19	7.45 \pm 0.12	146.34 \pm 2.62	42.51 \pm 1.26	340.71 \pm 1.46	327.82 \pm 6.36	380.17 \pm 1.38	203.16 \pm 1.91
EAVC RBF	48.12 \pm 0.34	11.23 \pm 0.16	79.18 \pm 0.56	10.65 \pm 0.17	333.23 \pm 0.81	216.01 \pm 21.97	328.80 \pm 0.58	184.38 \pm 0.82
GlobalMI RBF	39.09 \pm 0.31	11.85 \pm 0.15	102.67 \pm 0.43	22.34 \pm 0.35	311.79 \pm 0.51	253.46 \pm 30.79	332.62 \pm 0.60	205.70 \pm 1.04

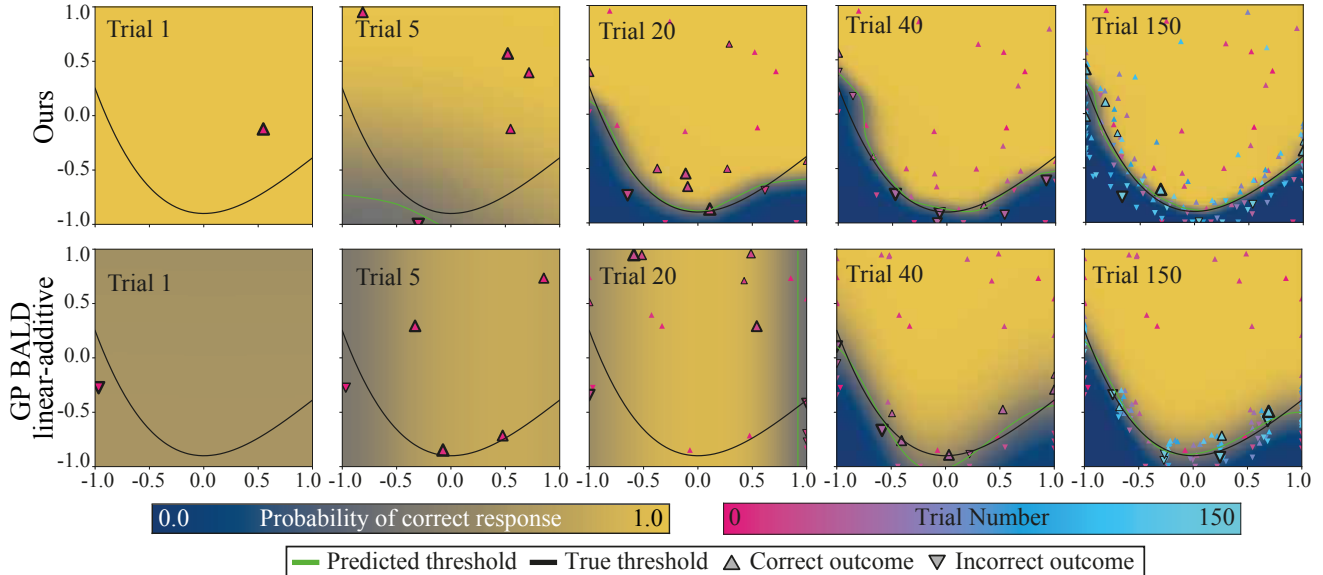


Figure 4: NEST and GP BALD linear-additive psychometric function estimation for the NV2D function after 1, 5, 20, 40, and 150 trials. Horizontal and vertical axes represent the input stimulus parameters. The ten most recent samples have a thicker border around the marker. Our method finds a relatively good approximation of the psychometric function after 20 trials.

tion 6.1) is a reproduction of the eccentricity-dependent spatial CSF, which serves as a test on a thoroughly studied 3D psychometric function. The second experiment (Section 6.2) is a reproduction of the spatio-temporal visibility model as a function of eccentricity by Tursun and Didyk (2022), which uses *virulent PEST* (vPEST) (Findlay, 1978). We observe that our method can estimate the psychometric functions from original studies with a high accuracy albeit with a smaller number of trials (Section 6.2).

In both experiments, the participants were positioned at a distance of 62 cm from the display. We used a 55-inch 4K LG OLED55CX display with a 120 Hz refresh rate and linear calibration. The peak spatial frequency of the display was 18.15 cycles per degree (cpd) and the peak luminance was set to 170 cd/m².

Each participant’s neural network is trained individually. A combined model representing the average psychometric function is obtained using *ensemble averaging* with equal weights, without additional training (Naftaly et al., 1997). The experiment procedure was approved by the research ethics committee of the hosting institution (CETO №. 95598952), and informed consent was obtained from each participant.

6.1. Spatial CSF experiment

In this experiment, we use sinusoidal Gabor gratings as the stimuli on a uniform gray background at 85 cd/m² luminance. The stimulus was presented at different retinal eccentricities $e \in [5^\circ, 30^\circ]$ with spatial frequencies $u \in [0.5, 9.07]$ cpd. The experiment task was to indicate whether the stimulus was on the left or the right side of

the visual field relative to a fixation target at the center. We compare our method with the model developed by Barten (1999) using retinal ganglion cell density formula from Watson (2014).

Six participants (3F, 3M), including one author, with mean age 27.2 ± 4.5 performed this experiment. All participants reported normal or corrected-to-normal vision. Figure 5 shows the results for participant C₁ as well as averaging all participants’ models in the spatial CSF experiment for eccentricities 5°, 10°, 15°, 20°, and 30°. The results for the other participants are provided in the supplementary material. The parameters of the Barten CSF model are shown in Table 4. The mean number of trials of our method was 353.8 ± 51.1 using our convergence criterion (Section 3 in suppl. mat.). The experiment took 20–35 minutes for each participant.

Figure 5 shows that many of the samples selected by NEST during the experiment are close to the final value of the detection threshold and that the samples are not clustered around a particular region (e.g., the stimulus space boundary), highlighting efficient sample selection. The results from a selected participant C₁ and the model fit to all participants’ responses are generally in agreement with the Barten’s CSF model.

Table 4: Parameters and values used for the CSF model by Barten (1999).

Parameter	Value	Parameter	Value
σ_0	1.5	r_e	7.633
e_g	3.3	η	0.04
k	2.3		

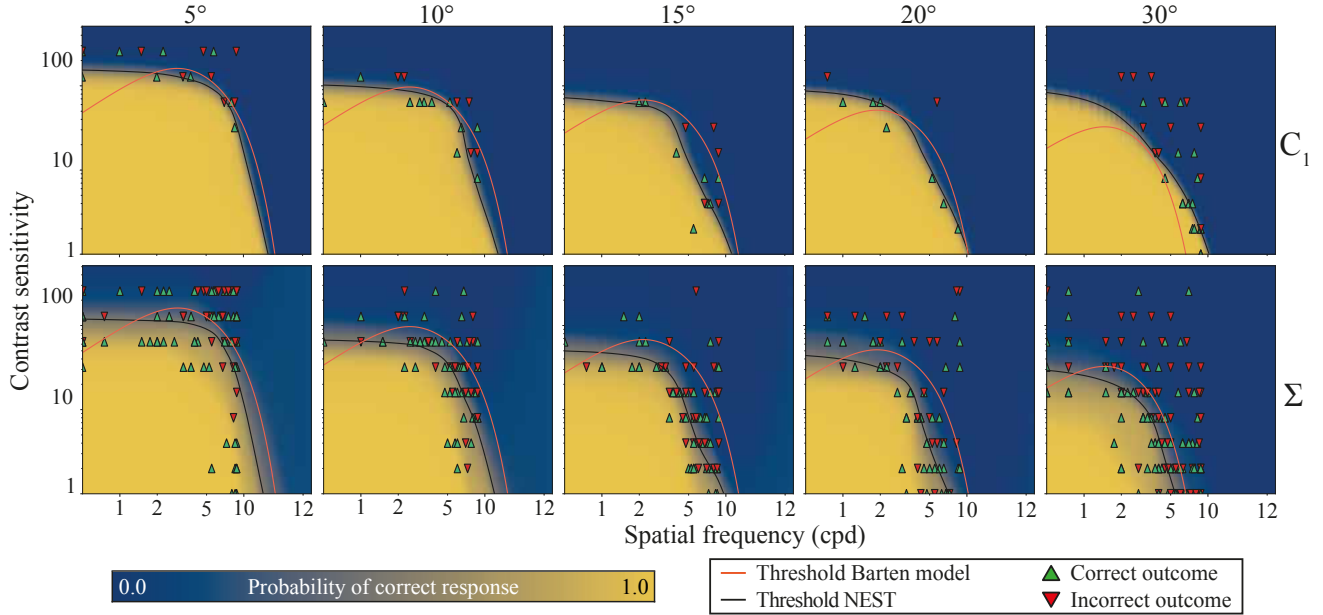


Figure 5: Psychometric function estimates from the CSF experiment (Section 6.1) for multiple eccentricities. The top row shows the model of participant C_1 and the bottom row (Σ) shows the average model of all participants. NEST learns a function that closely aligns with the fitted theoretical model.

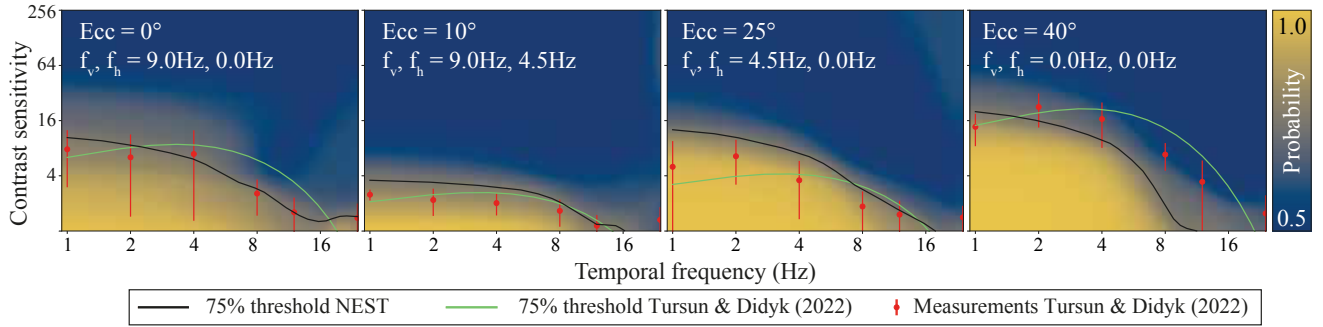


Figure 6: Selected 2D slices of the 5D psychometric function learned from the experiment discussed in Section 6.2. 75% detection threshold from the parameterized psychometric function introduced by Tursun and Didyk (2022) and their mean sensitivity measurements are shown in green and red, respectively. The predicted threshold by NEST is shown in black. We observe that NEST is able to capture trends of the data better than the model of Tursun and Didyk (2022). Vertical bars represent standard error of the mean.

6.2. Spatio-temporal visibility model experiment

The second experiment is a reproduction of the perceptual visibility model as a function of spatio-temporal frequency and eccentricity (Tursun and Didyk, 2022), which uses vPEST (Findlay, 1978). Due to the high dimensionality, their procedure limited the number of unique stimulus values in each dimension to just three. Nevertheless, the authors report an average duration of 240 minutes for each participant in multiple sessions. For each of the 162 stimulus combinations, a separate vPEST procedure was run, and the total number of trials for each participant was approximately 5,000.

Five participants (2F, 3M), including one author, with mean age 23.4 ± 2.5 performed this experiment. Figure 6 shows the results found by combining the individual re-

sults of all the participants P1–P5 in this experiment. The individual results are shown in the supplementary material. The experiment took an average of 730.8 ± 65.6 trials with our method to reach convergence, which took 60–80 minutes for each participant. Both the number of trials and experiment duration is significantly reduced with our method.

Figure 6 shows the psychometric function learned by NEST for all combined participants, as well as the original data collected by Tursun and Didyk (2022) and their model fit. Due to its non-parametric nature, we observe that NEST has more flexibility in coming up with a better fit to the measurements with significantly fewer trials.

7. Ablation study

We perform Monte Carlo simulations with subsets of components from the acquisition function and report the AUC from RMSE and Brier score in Table 5. We group the best AUC scores that are statistically different from the rest ($p \leq 0.05$, Dunnett test). Different subsets of the acquisition function components seem to achieve good results for estimating particular psychometric functions. For example, proximity and uncertainty components for NV2D, the combination of gradient, proximity, and uncertainty for SIN2D, and lookahead component for HART6 were critical for an efficient estimation of the psychometric function. In order to achieve the best scores overall for all tested psychometric functions and metrics, we observe that using all four components of the acquisition function is crucial.

8. Discussion and limitations

Our benchmarks in Section 5 assume that the input space is continuous, but in practice we often use discrete sampling to improve running time. We observed that coarse discrete sampling of the stimulus space for sample selection has minimal impact on the performance (see the supplementary material for details).

Being a non-parametric model, our psychometric function estimate does not in general allow for extrapolation outside the stimulus space boundaries used in experiments. In the experiment shown in Figure 5, our display was capable of rendering spatial frequencies up to the Nyquist limit 9.07 cpd. Due to our regularization scheme, we observed that the learned psychometric function outputs changed smoothly for spatial frequencies higher than the limit imposed by the display hardware. As a future work, we believe that the model generalization may be improved by optimizing the regularization parameters.

Table 5: The ablation mean AUC \pm standard error of the RMSE and Brier metrics for the NV2D, WEI4D, and HART6 functions. Each row indicates the included components, Uncertainty (U), Proximity (P), Gradient (G), and Lookahead (L). For the ‘‘Random’’ category, Poisson-disk random sampling (Wang, 2020) is used as a pure random exploration behavior as a reference. The group of best scores that lack a significant difference ($p \leq 0.05$, Dunnett test) are shown in boldface.

Method	NV2D		SIN2D		DN2D		WEI4D		HART6	
	AUC _{RMSE}	AUC _{Brier}	AUC _{RMSE}	AUC _{Brier}	AUC _{RMSE}	AUC _{Brier}	AUC _{RMSE}	AUC _{Brier}	AUC _{RMSE}	AUC _{Brier}
Random	34.75 \pm 0.31	9.95 \pm 0.14	62.77 \pm 0.30	22.52 \pm 0.23	51.45 \pm 0.29	22.38 \pm 0.21	75.39 \pm 0.52	12.31 \pm 0.17	263.11 \pm 1.38	128.83 \pm 1.39
U	37.10 \pm 0.46	11.17 \pm 0.24	72.42 \pm 0.50	26.15 \pm 0.39	64.08 \pm 0.82	29.70 \pm 0.65	43.92 \pm 0.30	8.19 \pm 0.12	270.08 \pm 2.96	149.43 \pm 3.40
P	32.63 \pm 0.34	9.60 \pm 0.16	67.92 \pm 0.36	26.59 \pm 0.27	57.76 \pm 0.41	26.09 \pm 0.23	72.00 \pm 0.52	11.78 \pm 0.16	255.58 \pm 1.40	125.17 \pm 1.39
P + U	24.63 \pm 0.24	6.86 \pm 0.11	62.26 \pm 0.37	23.75 \pm 0.35	50.95 \pm 0.53	23.20 \pm 0.28	43.31 \pm 0.32	7.92 \pm 0.12	252.70 \pm 2.67	123.47 \pm 2.61
G	43.81 \pm 0.78	12.70 \pm 0.32	77.93 \pm 0.51	28.74 \pm 0.35	73.79 \pm 0.52	34.39 \pm 0.62	44.59 \pm 0.33	8.76 \pm 0.15	316.00 \pm 2.14	161.20 \pm 2.11
G + U	39.52 \pm 0.47	12.14 \pm 0.26	71.48 \pm 0.50	26.07 \pm 0.38	63.93 \pm 0.44	29.03 \pm 0.60	44.23 \pm 0.30	8.06 \pm 0.11	268.69 \pm 2.75	144.30 \pm 2.86
G + P	29.03 \pm 0.35	8.28 \pm 0.15	65.29 \pm 0.38	25.04 \pm 0.28	53.93 \pm 0.44	23.88 \pm 0.25	42.56 \pm 0.36	8.02 \pm 0.13	309.82 \pm 2.10	157.56 \pm 2.09
G + P + U	23.41 \pm 0.20	6.44 \pm 0.10	59.98 \pm 0.30	21.98 \pm 0.20	49.83 \pm 0.40	22.61 \pm 0.20	44.06 \pm 0.27	8.11 \pm 0.12	262.87 \pm 2.49	129.89 \pm 2.29
L	47.11 \pm 1.04	13.53 \pm 0.42	63.86 \pm 0.41	23.62 \pm 0.26	55.46 \pm 0.38	24.80 \pm 0.25	58.61 \pm 0.46	9.42 \pm 0.14	295.62 \pm 2.70	132.87 \pm 2.59
L + U	28.08 \pm 0.32	6.94 \pm 0.12	65.34 \pm 0.39	23.68 \pm 0.28	58.91 \pm 0.67	26.45 \pm 0.54	45.40 \pm 0.31	8.01 \pm 0.12	238.34 \pm 2.26	104.88 \pm 2.17
L + P	29.85 \pm 0.29	8.34 \pm 0.14	68.34 \pm 0.39	26.97 \pm 0.28	58.42 \pm 0.44	26.36 \pm 0.24	58.15 \pm 0.39	8.88 \pm 0.12	277.55 \pm 2.26	119.91 \pm 2.10
L + P + U	23.85 \pm 0.22	6.38 \pm 0.10	62.66 \pm 0.34	23.79 \pm 0.24	50.72 \pm 0.58	22.88 \pm 0.30	45.91 \pm 0.26	8.33 \pm 0.11	238.75 \pm 2.30	106.87 \pm 2.26
L + G	46.80 \pm 0.98	13.43 \pm 0.42	65.20 \pm 0.47	23.82 \pm 0.28	56.90 \pm 0.57	24.28 \pm 0.32	44.83 \pm 0.29	8.32 \pm 0.11	307.36 \pm 2.79	144.13 \pm 2.61
L + G + U	28.85 \pm 0.31	7.37 \pm 0.12	65.04 \pm 0.44	23.73 \pm 0.30	60.17 \pm 0.76	26.99 \pm 0.62	45.26 \pm 0.30	8.29 \pm 0.11	249.04 \pm 2.35	113.29 \pm 2.22
L + G + P	28.10 \pm 0.31	7.75 \pm 0.14	65.47 \pm 0.36	25.00 \pm 0.26	53.35 \pm 0.46	23.46 \pm 0.25	43.68 \pm 0.28	8.05 \pm 0.11	294.13 \pm 2.88	134.17 \pm 2.77
Full	23.29 \pm 0.20	6.25 \pm 0.09	60.23 \pm 0.29	22.08 \pm 0.0.22	50.00 \pm 0.40	22.68 \pm 0.24	44.05 \pm 0.25	8.10 \pm 0.12	246.52 \pm 2.64	108.75 \pm 2.19

9. Conclusion

In this study, we introduced a neural network-based psychophysical procedure called *Neural Estimation by Sequential Testing* (NEST). The aim of using a neural network was to: (1) expand existing psychophysical procedures for high-dimensional problems; (2) free the experimenter from the requirement of choosing a parametric form in the fitting process required by the QUEST+ procedure, or a kernel function as in the GP methods; and (3) improve the state-of-the-art performance for high-dimensional psychometric function estimation with a Bernoulli response variable. We showed that NEST is able to outperform QUEST+ in high-dimensional problems, and that it performs better overall on psychometric function estimation than the state-of-the-art GP methods. Subsequently, we demonstrated that our network is practically applicable for high-dimensional psychovisual experiments: firstly, we established that we could recover the CSF function as a function of spatial frequency and of eccentricity within a reasonable experimentation time. Secondly, we showed that for a selected high-dimensional psychovisual experiment, using NEST significantly reduced the number of trials and the amount of time needed to perform the experiment, while achieving better fits. These results show that NEST offers significant benefits for conducting multi-dimensional psychovisual experiments.

CRedit authorship contribution statement

Sjoerd Bruin: methodology, investigation, formal analysis, data curation, visualization, validation, software, writing - original draft. **Jiří Kosinka:** conceptualization, supervision, writing - review & editing. **Cara Tursun:** conceptualization, supervision, writing - review & editing

Declaration of competing interest

The authors declare that there are no competing financial interests or personal relationships that could have influenced the work in this paper.

References

- Ash, J.T., Adam, R.P., 2020. On warm-starting neural network training, in: NIPS'20: Proceedings of the 34th International Conference on Neural Information Processing Systems, p. 3884–3894. doi:10.5555/3495724.3496051.
- Barten, P.G.J., 1999. Contrast sensitivity of the human eye and its effects on image quality. SPIE Optical Engineering Press.
- Brier, G.W., 1950. Verification of forecasts expressed in terms of probability. *Monthly Weather Review* 78, 1–3. doi:10.1175/1520-0493(1950)078<0001:V0FEIT>2.0.CO;2.
- Dubno, J.R., Eckert, M.A., Lee, F.S., Matthews, L.J., Schmiedt, R.A., 2013. Classifying human audiometric phenotypes of age-related hearing loss from animal models. *Journal of the Association for Research in Otolaryngology* 14, 687–701. doi:10.1007/s10162-013-0396-x.
- Emerson, P.L., 1986. Observations on maximum-likelihood and Bayesian methods of forced-choice sequential threshold estimation. *Perception & Psychophysics* 39, 151–153. doi:10.3758/BF03211498.
- Fedorov, V.V., 2013. Theory of optimal experiments. Elsevier.
- Findlay, J.M., 1978. Estimates on probability functions: A more virulent PEST. *Perception & Psychophysics* 23, 181–185. doi:10.3758/BF03208300.
- Gal, Y., Ghahramani, Z., 2016. Dropout as a Bayesian approximation: Representing model uncertainty in deep learning, in: ICML'16: Proceedings of the 33rd International Conference on International Conference on Machine Learning, pp. 1050–1059.
- Games, P.A., Howell, J.F., 1976. Pairwise multiple comparison procedures with unequal N's and/or variances: A Monte Carlo study. *Journal of Educational and Behavioral Statistics* 1, 113–125. doi:10.3102/10769986001002113.
- García-Pérez, M.A., 2014. Adaptive psychophysical methods for non-monotonic psychometric functions. *Attention, Perception, & Psychophysics* 76, 621–641.
- Gardner, J.R., Song, X.D., Weinberger, K.Q., Barbour, D.L., Cunningham, J.P., 2015. Psychophysical detection testing with Bayesian active learning, in: 31st Conference on Uncertainty in Artificial Intelligence, Association for Uncertainty in Artificial Intelligence. pp. 286–295.
- Gotovos, A., Casati, N., Hitz, G., Krause, A., 2013. Active learning for level set estimation, in: Proceedings of the Twenty-Third International Joint Conference on Artificial Intelligence, International Joint Conferences on Artificial Intelligence. pp. 1344–1350. doi:10.5555/2540128.2540322.
- Green, D.M., Luce, R.D., 1975. Parallel psychometric functions from a set of independent detectors. *Psychological Review* 82, 483.
- He, K., Zhang, X., Ren, S., Sun, J., 2015. Delving deep into rectifiers: Surpassing human-level performance on ImageNet classification, in: 2015 IEEE International Conference on Computer Vision (ICCV), pp. 1026–1034. doi:10.1109/ICCV.2015.123.
- Hinton, G.E., Srivastava, N., Krizhevsky, A., Sutskever, I., Salakhutdinov, R.R., 2012. Improving neural networks by preventing co-adaptation of feature detectors. doi:10.48550/arXiv.1207.0580. arxiv preprint.
- Hornik, K., Stinchcombe, M., White, H., 1989. Multilayer feedforward networks are universal approximators. *Neural networks* 2, 359–366.
- Houlsby, N., Hernández-Lobato, J., Huszár, F., Ghahramani, Z., 2012. Collaborative Gaussian processes for preference learning, in: Advances in Neural Information Processing Systems, NeurIPS. pp. 1–9.
- King-Smith, P.E., Grigsby, S.S., Vingrys, A.J., Benes, S.C., Supowit, A., 1994. Efficient and unbiased modifications of the QUEST threshold method: Theory, simulations, experimental evaluation and practical implementation. *Vision Research* 34, 885–912. doi:10.1016/0042-6989(94)90039-6.
- Kingma, D.P., Ba, J., 2014. Adam: A method for stochastic optimization. CoRR abs/1412.6980.
- Klein, S.A., 2001. Measuring, estimating, and understanding the psychometric function: A commentary. *Perception & psychophysics* 63, 1421–1455.
- Kontsevich, L.L., Tyler, C.W., 1999. Bayesian adaptive estimation of psychometric slope and threshold. *Vision Research* 39, 2729–2737. doi:10.1016/S0042-6989(98)00285-5.
- Leek, M.R., 2001. Adaptive procedures in psychophysical research. *Perception & psychophysics* 63, 1279–1292.
- Lesmes, L.A., Jeon, S.T., Lu, Z.L., Doshier, B.A., 2006. Bayesian adaptive estimation of threshold versus contrast external noise functions: the quick TvC method. *Vision Research* 46, 3160–3176. doi:10.1016/j.visres.2006.04.022.
- Lesmes, L.A., Lu, Z.L., Baek, J., Albright, T.D., 2010. Bayesian adaptive estimation of the contrast sensitivity function: The quick CSF method. *Journal of Vision* 12, 17:1–17:21. doi:10.1167/10.3.17.
- Letham, B., Guan, P., Tymms, C., Bakshy, E., Shvartsman, M., 2022. Look-ahead acquisition functions for Bernoulli level set estimation, in: International Conference on Artificial Intelligence and Statistics, PMLR. pp. 8493–8513.
- Lewis, D.D., Catlett, J., 1994. Heterogeneous uncertainty sampling for supervised learning, in: Machine learning proceedings 1994. Elsevier, pp. 148–156.
- Liao, Z., Drummond, T., Reid, I., Carneiro, G., 2020. Approximate Fisher information matrix to characterize the training of deep neural networks. *IEEE Transactions on Pattern Analysis and Machine Intelligence* 42, 15–26.
- Lyu, X., Binois, M., Ludkovski, M., 2021. Evaluating Gaussian process metamodels and sequential designs for noisy level set estimation. *Statistics and Computing* 31, 43:1–21. doi:10.1007/s11222-021-10014-w.
- Ma, L., Kaewell, J., 2020. Fast Monte Carlo dropout and error correction for radio transmitter classification, in: 2020 IEEE International Workshop on Information Forensics and Security (WIFS), pp. 1–5. doi:10.1109/WIFS49906.2020.9360887.
- MacKay, D.J., 1992. Information-based objective functions for active data selection. *Neural computation* 4, 590–604.
- MacKay, D.J., 1998. Introduction to Gaussian processes. NATO ASI Series F Computer and Systems Sciences 168, 133–166.
- Mohamadi, M.A., Bae, W., Sutherland, D.J., 2022. Making look-ahead active learning strategies feasible with neural tangent kernels. *Advances in Neural Information Processing Systems* 35, 12542–12553.
- Nachmias, J., 1981. On the psychometric function for contrast detection. *Vision research* 21, 215–223.
- Naftaly, U., Intrator, N., Horn, D., 1997. Optimal ensemble averaging of neural networks. *Network: Computation in Neural Systems* 8, 283–296. doi:10.1088/0954-898X_8_3_004.
- Nair, V., Hinton, G.E., 2010. Rectified linear units improve restricted Boltzmann machines, in: ICML'10: Proceedings of the 27th International Conference on International Conference on Machine Learning, p. 807–814. doi:10.5555/3104322.3104425.
- Owen, L., Browder, J., Letham, B., Stocck, G., Tymms, C., Shvartsman, M., 2021. Adaptive nonparametric psychophysics. doi:10.48550/ARXIV.2104.09549.
- Paszke, A., Gross, S., Massa, F., 2019. PyTorch: An imperative style, high-performance deep learning library, in: 33rd Conference on Neural Information Processing Systems, NeurIPS. p. 8026–8037.
- Rosenblatt, F., 1961. Principles of Neurodynamics: Perceptrons and the Theory of Brain Mechanisms. Spartan Books.
- Settles, B., 2009. Active Learning Literature Survey. volume 1648 of *Computer Sciences Technical Report*. University of Wisconsin–Madison.
- Settles, B., 2012. Uncertainty Sampling. Springer International Publishing, Cham. chapter Uncertainty Sampling. pp. 11–20. doi:10.1007/978-3-031-01560-1_2.
- Shahriari, B., Swersky, K., Wang, Z., Adams, R.P., De Freitas, N., 2015. Taking the human out of the loop: A review of Bayesian optimization. *Proceedings of the IEEE* 104, 148–175.
- Sietsma, J., Dow, R.J.F., 1991. Creating artificial neural networks that generalize. *Neural Networks* 4, 67–79. doi:10.1016/0893-6080(91)90033-2.
- Siivola, E., Vehtari, A., Vanhatalo, J., Gonzales, J., Andersen, M.R., 2018. Correcting boundary over-exploration deficiencies in

- Bayesian optimization with virtual derivation sign observations, in: 2018 IEEE 28th International Workshop on Machine Learning for Signal Processing (MLSP), pp. 1–6. doi:10.1109/MLSP.2018.8516936.
- Song, X.D., Sukesan, K.A., Barbour, D.L., 2018. Bayesian active probabilistic classification for psychometric field estimation. *Attention, Perception & Psychophysics* 80, 798–812. doi:10.3758/s13414-017-1460-0.
- Song, X.D., Wallace, B.M., Gardner, J.R., Ledbetter, N.M., Weinberger, K.Q., Barbour, D.L., 2015. Fast, continuous audiogram estimation using machine learning. *Ear Hear* 36, e326–e335. doi:10.1097/AUD.0000000000000186.
- Srivastava, N., Hinton, G., Krizhevsky, A., Sutskever, I., Salakhutdinov, R., 2014. Dropout: a simple way to prevent neural networks from overfitting. *The journal of machine learning research* 15, 1929–1958.
- Treutwein, B., 1995. Adaptive psychophysical procedures. *Vision Research* 35, 2503–2522. doi:10.1016/0042-6989(95)00016-X.
- Tursun, C., Didyk, P., 2022. Perceptual visibility model for temporal contrast changes in periphery. *ACM Transactions on Graphics* 42, 20:1–16. doi:10.1145/3564241.
- Virtanen, P., Gommers, R., Oliphant, T.E., Haberland, M., Reddy, T., Cournapeau, D., Burovski, E., Peterson, P., Weckesser, W., Bright, J., Van der Walt, S.J., Brett, M., Wilson, J., Millman, K.J., Mayorov, N., Nelson, A.R.J., Jones, E., Kern, R., Larson, E., Carey, C.J., Polat, I., Feng, Y., Moore, E.W., VanderPlas, J., Laxalde, D., Perktold, J., Cimrman, R., Henriksen, I., Quintero, E.A., Harris, C.R., Archibald, A.M., Ribeiro, A.H., Pedregosa, F., Van Mulbregt, P., other SciPy contributors, 2020. SciPy 1.0: Fundamental Algorithms for Scientific Computing in Python. *Nature Methods* 17, 261–272. doi:10.1038/s41592-019-0686-2.
- Vul, E., Bergsma, J., Macleod, D.I.A., 2010. Functional adaptive sequential testing. *Seeing & Perceiving* 23, 483–515. doi:10.1163/187847510x532694.
- Wang, T., 2020. Poisson-disk sampling: Theory and applications, in: *Encyclopedia of Computer Graphics and Games*, Springer International Publishing. pp. 1–8. doi:10.1007/978-3-319-08234-9_398-1.
- Watson, A.B., 2014. A formula for human retinal ganglion cell receptive field density as a function of visual field location. *Journal of Vision* 14, 15:1–17. doi:10.1167/14.7.15.
- Watson, A.B., 2017. QUEST+: A general multidimensional Bayesian adaptive psychometric method. *Journal of Vision* 17, 10:1–10:27. doi:10.1167/17.3.10.
- Watson, A.B., Ahumada, A.J., 2016. The pyramid of visibility, in: *Proc. IS&T Int'l. Symp. on Electronic Imaging: Human Vision and Electronic Imaging*, pp. 16:1–6. doi:10.2352/ISSN.2470-1173.2016.16.HVEI-102.
- Watson, A.B., Pelli, D.G., 1983. QUEST: A Bayesian adaptive psychometric method. *Perception & Psychophysics* 33, 113–120. doi:10.3758/BF03202828.
- Weibull, W., 1951. A statistical distribution function of wide applicability. *Journal of Applied Mechanics* 18, 293–297.

Supplementary Material for NEST: Neural Estimation by Sequential Testing

Sjoerd Bruin^{a,*}, Jiří Kosinka^a, Cara Tursun^a

^a*Bernoulli Institute, University of Groningen, Nijenborgh 9, Groningen, 9747AG, The Netherlands*

arXiv:2405.04226v1 [stat.ME] 7 May 2024

1. Definition of Hartmann6 psychometric function

We use a similar notation as Letham et al. (2022). The 6D Hartmann (HART6) function is given by

$$h(\vec{x}) = 1 - \sum_{i=1}^4 \alpha_i e^{-\sum_{j=1}^6 A_{ij}(x_j - P_{ij})^2}, \quad (1)$$

where $\vec{\alpha} = (2.0, 2.2, 2.8, 3.0)$,

$$A = \begin{pmatrix} 8 & 3 & 10 & 3.5 & 1.7 & 6 \\ 0.5 & 8 & 10 & 1.0 & 6 & 9 \\ 3 & 3.5 & 1.7 & 8 & 10 & 6 \\ 10 & 6 & 0.5 & 8 & 1.0 & 9 \end{pmatrix}, \text{ and}$$

$$P = 10^{-4} \begin{pmatrix} 1312 & 1696 & 5569 & 124 & 8283 & 5886 \\ 2329 & 4135 & 8307 & 3736 & 1004 & 9991 \\ 2348 & 1451 & 3522 & 2883 & 3047 & 6650 \\ 4047 & 8828 & 8732 & 5743 & 1091 & 381 \end{pmatrix}.$$

HART6 is defined on the range $\vec{x} \in [0, 1]^6$. We follow Letham et al. (2022) in rescaling HART6 as

$$f(\vec{x}) = 3h(\vec{x}) - 2 \quad (2)$$

in order to make the comparison with Letham et al. (2022) as close as possible. We convert the function $f(\vec{x})$ into a probability of detection by passing it into the standard Gaussian CDF $\Phi(\cdot)$ and scaling by the lower asymptote and lapse as

$$\Psi(\vec{x}, \alpha, \gamma) = \alpha + (1 - \alpha - \gamma)\Phi(f(\vec{x})). \quad (3)$$

2. Sample Selection

Figure 1 in Suppl. Mat. shows the gradient, proximity, uncertainty, and lookahead components of the query generation function discussed in Section 2.2, as well as the combined product term. The gradient term visualised in Figure 1 in Suppl. Mat. reaches a maximum value at the steepest point along the transition region, which is the expected behaviour. The uncertainty term has a larger

value near the edges of the input space, which is expected since there is more uncertainty at those places due to the unknown distribution outside the input space. The lookahead term finds its highest points along the transition region, which makes sense since the predicted minimum impact of a label of either sign is largest there. Additionally, the lookahead component picks out locations along the boundary that have not been explored as much as other regions.

At step 20, the proximity term has a somewhat random distribution. At step 90, on the other hand, it is clear that the samples have been selected along the predicted transition boundary, and as a consequence, the proximity term is large along this boundary. For the final product, this means that there is a strong discouraging effect from sampling many more samples along the boundary, which is counterbalanced by the high gradient and uncertainty terms. As a result, the final product term at step 20 is mostly focused on exploring the transition boundary, whereas at step 90 it is more likely to select points away from the transition boundary while retaining a propensity to select samples towards the middle of the transition region.

3. Convergence Criterion

For analyzing convergence, we computed the Fisher energy progression for 100 runs for 2D-6D Weibull functions and also for the sphere function, which defines a radius r against which the size of the input vector \vec{x} is tested as a measure of the threshold. The definition is given by

$$\Psi(\vec{x}, \beta, r, \alpha, \gamma) = \alpha + (1 - \gamma - \alpha)e^{-10^\beta \frac{\|\vec{x}\|_2 - r}{20}}, \quad (4)$$

where $\|\vec{x}\|_2$ indicates the Euclidean distance of the stimulus from the center of the input space. A single 1-dimensional slope parameter β is used in this function. We used a radius equal to $\frac{1}{4}$ of the input space dimensions. Additionally, we created a baseline for the Fisher energy using a multi-dimensional psychometric function that gave random responses all the time. Rather than looking at the absolute size of the Fisher energy, we study how much the Fisher energy changes from one trial to the next. We monitor a window of 15 difference values, and study how this

*Corresponding author. Email address: s.bruin@rug.nl

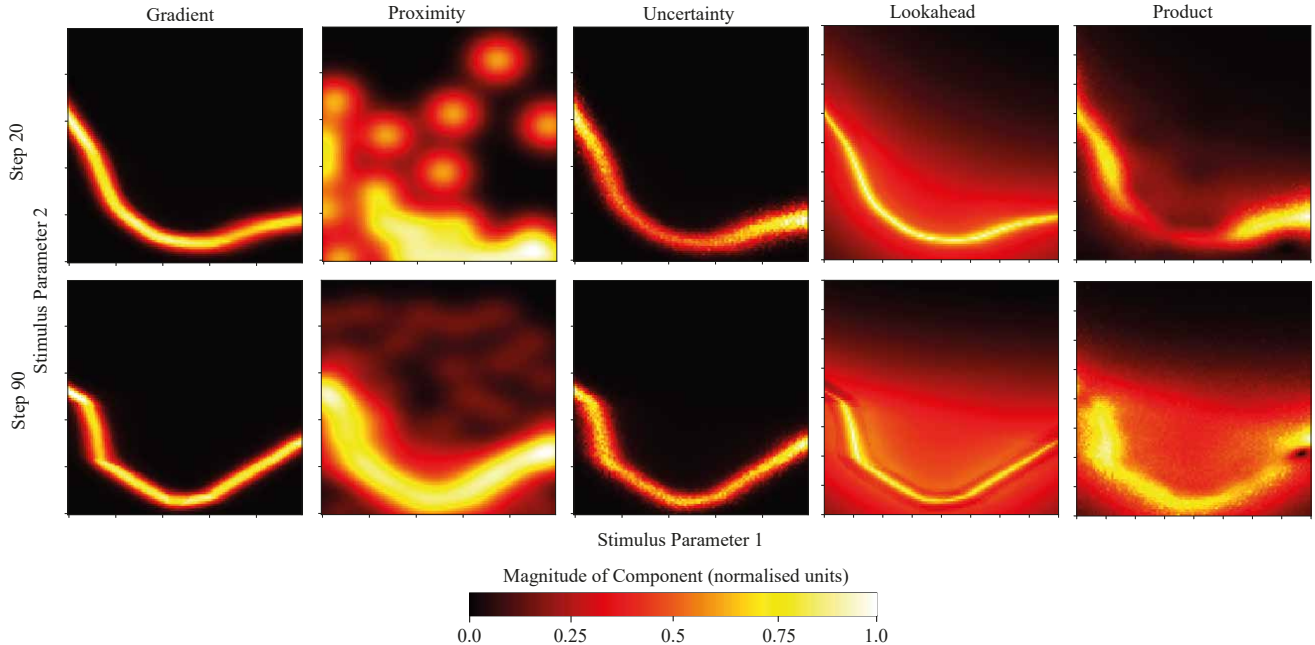


Figure 1: Visualisation of the components of the acquisition function for the NV2D function. At 20 samples, the algorithm encourages exploration around the estimated boundary, but at 90 samples, more emphasis is given to the space at the edges of the transition region.

window converges. Our aim is to suggest a useful heuristic for terminating an experiment.

Table 1 in Suppl. Mat. shows the Spearman rank correlation between the RMSE errors in the validation set and the Fisher energy computed on the training set. We use the Spearman rank correlation because the relationship has a logarithmic character, and therefore the Pearson correlation would miss the relationship between the variables. The correlation shows that there is a strong association between the Fisher energy and the generalization error, which makes it a useful heuristic for suggesting termination.

In order to suggest quantitative termination criteria, we looked at the correspondence between the Fisher energy of a simulation with completely random responses and a simulation of a well-defined psychometric function using the Sphere and Weibull psychometric functions. The results are shown in Figure 2 in Suppl. Mat.

Several observations arise from Figure 2 in Suppl. Mat.

Table 1: The Spearman rank correlation between the RMSE on the validation set and the Fisher energy for the training set. The correlation is very strong, indicating that the Fisher energy is a good predictor of the achieved generalization error.

Dimension	Weibull	Sphere
2D	0.9843	0.9790
3D	0.9902	0.9848
4D	0.9705	0.8431
5D	0.7931	0.9107
6D	0.8874	0.9717

Firstly, the Fisher energy decreases as the number of dimensions increases. This suggests that we need to recommend a convergence criterion based on the dimensionality of the input space. Figure 2 in Suppl. Mat. further shows that there is a converging ratio between the Fisher energy of the random function and those of non-random functions. The ratio, which we call the *signal-to-noise ratio* (SNR), appears to trend towards a value of 10 in most cases. This value makes for a suitable cut-off for our windowed Fisher energy value. We have used this value to assess convergence during the live experiments discussed in Sections 6.1 and 6.2. We have found that the results of the experiment did not change noticeably when one of the authors continued the experiment after Fisher energy convergence had been reached. This shows that the criterion reflects a suitable level of convergence for NEST. If a higher confidence in the final result is needed, then a lower SNR value can be chosen. The approximate baseline Fisher energy difference levels from the random simulation that we have found are given in Table 2 in Suppl. Mat. We found these values to be useful guides for the termination condition in the psychovisual experiments that we have performed.

4. The shrink-and-perturb operation

As mentioned in the main paper, we use the *shrink-and-perturb* trick for warm-starting, introduced by Ash and Adams (2020), in order to avoid overfitting and to increase the stability between trials. This method shrinks the size of each weight parameter and adds a small amount

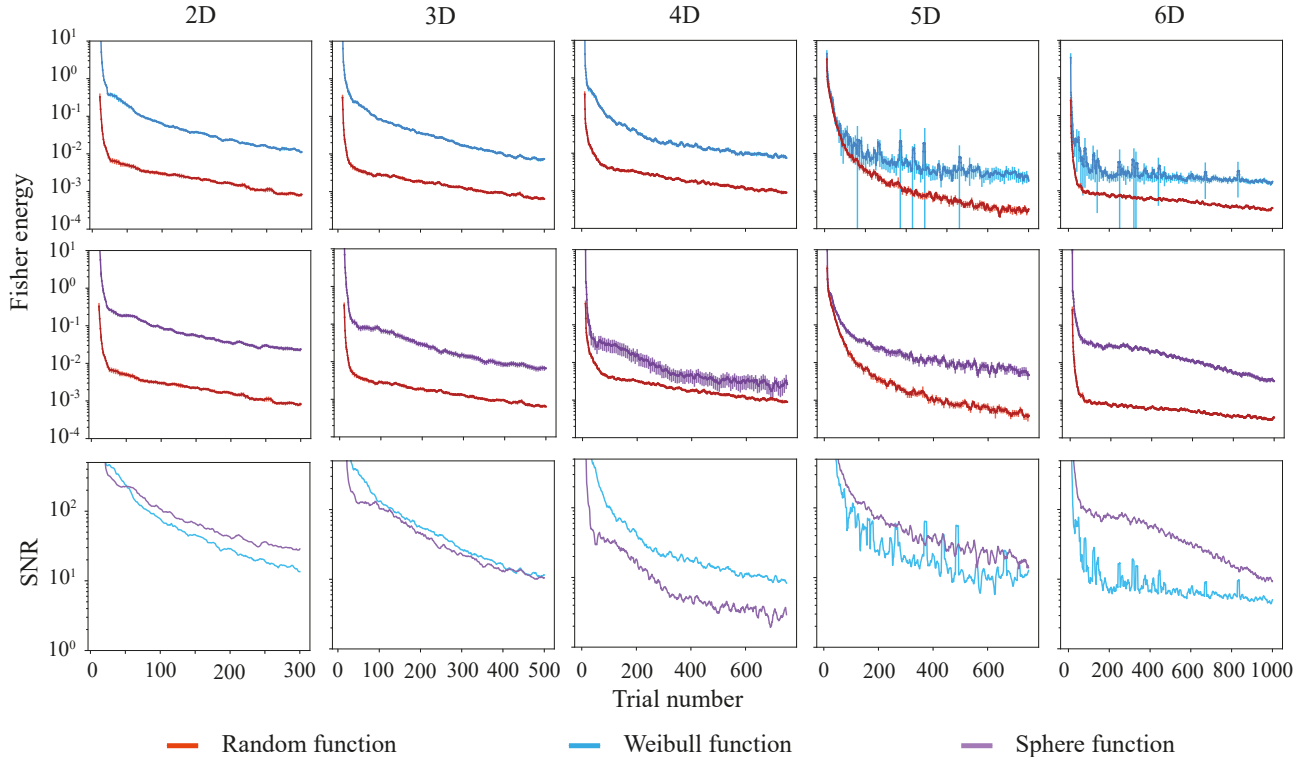


Figure 2: 15-trial windowed Fisher energy and 95% confidence interval of a psychometric function with random responses, the Weibull psychometric function, and the sphere psychometric function. The mean SNR value versus the random function trends down towards a similar value for both psychometric functions, which supports the use of the SNR value as a useful heuristic for assessing convergence.

of random noise at the beginning of the training by

$$W_t(i, j) \leftarrow \lambda W_t(i, j) + p, \quad (5)$$

where λ is the shrink parameter, $p \sim \mathcal{N}(0, \epsilon_{\text{per}}^2)$, and ϵ_{per} is the standard deviation of the noise used to perturb the weights. In our experiments, we set $\lambda = 0.9$ and $\epsilon_{\text{per}} = 0.01$.

5. Discrete Sample Robustness

The NEST algorithm assumes that we can select samples for evaluation from a continuous space, but this assumption does not always hold, for example if the stimuli in an experiment can only be generated at fixed step sizes. We study the impact of discrete sample selection on the accuracy of the method in this section. Af-

ter finding an optimal sample location in the continuous sample space, we snap the selected location to the nearest discrete sample and evaluate that location. We set $n_{\text{sample}} \in \{4, 8, 16, 32, 64, 128, 256, 512\}$, where n_{sample} represents the number of sample locations in each dimension.

Table 3 in Suppl. Mat. and Figure 3 in Suppl. Mat. show the errors for NV2D, DN2D, SIN2D, WEI4D, and HART6. Using only 4, 8, or 16 samples per dimension leads to a significantly decreased performance. Starting at 32 samples, however, the results become very close to the continuous sample selection case. This shows that our method is robust against discretization of trial samples.

6. Other Results

In the rest of the Supplementary Materials, we provide a number of additional results to support the conclusions in the main paper. Table 4 in Suppl. Mat. and Table 5 in Suppl. Mat. show the AUC values for the RMSE and Brier score for all tested functions. The plotted error curves accompanying these tables are shown in Figure 4 in Suppl. Mat. and Figure 5 in Suppl. Mat. We evaluate the experiments on both *detection* ($\alpha = 0.0$) and *2-alternative forced choice* (2AFC) or *discrimination* ($\alpha = 0.5$) versions of the synthetic psychometric functions, in order to show that NEST can also handle problems where the lower asymp-

Table 2: Baseline windowed Fisher energy difference levels determined for the random psychometric function.

Dimension	Windowed Fisher energy difference
2D	$9 \cdot 10^{-4}$
3D	$7 \cdot 10^{-4}$
4D	$6 \cdot 10^{-4}$
5D	$5 \cdot 10^{-4}$
6D	$4 \cdot 10^{-4}$

tote is different from 0. Figure 6 in Suppl. Mat. shows the graphed ablation results.

Finally, Figure 7 in Suppl. Mat. shows the estimated psychometric functions for the Barten CSF experiment described in Section 6.1, including the individual psychometric functions of each participant as well as the combined psychometric function. Figures 8 in Suppl. Mat. and onwards show the expanded results of the spatio-temporal experiment in Section 6.2.

Table 3: The mean AUC \pm standard error for the discrete sampling experiments using the RMSE and Brier metrics for the NV2D, DN2D, SIN2D, WEI4D, and HART6 functions. The best method and methods that are statistically similar ($p \geq 0.05$, Games-Howell test) to it are shown in bold typeface for each metric. Using 32 samples is typically enough to get close to the performance of the continuous form of the acquisition function.

Method	NV2D		DN2D		SIN2D		WEI4D		HART6	
	AUC _{RMSE}	AUC _{Brier}	AUC _{RMSE}	AUC _{Brier}	AUC _{RMSE}	AUC _{Brier}	AUC _{RMSE}	AUC _{Brier}	AUC _{RMSE}	AUC _{Brier}
Continuous	21.83 \pm 0.23	7.56 \pm 0.11	24.05 \pm 1.01	6.25 \pm 0.21	67.21 \pm 0.32	25.25 \pm 0.20	64.89 \pm 1.13	13.62 \pm 0.35	277.51 \pm 1.87	148.15 \pm 2.81
4 samples	84.56 \pm 1.69	42.88 \pm 0.99	71.94 \pm 0.64	26.87 \pm 0.45	141.14 \pm 0.51	75.79 \pm 0.54	196.31 \pm 3.81	53.86 \pm 1.50	320.20 \pm 2.54	232.36 \pm 4.08
8 samples	36.43 \pm 0.68	12.50 \pm 0.33	52.87 \pm 1.10	16.07 \pm 0.42	103.92 \pm 0.82	51.39 \pm 0.68	107.62 \pm 1.88	25.20 \pm 0.68	311.34 \pm 2.89	215.79 \pm 3.78
16 samples	27.50 \pm 0.34	8.61 \pm 0.19	32.29 \pm 0.97	8.57 \pm 0.21	79.24 \pm 1.16	32.70 \pm 0.75	77.03 \pm 1.24	16.42 \pm 0.40	300.69 \pm 2.00	192.55 \pm 3.04
32 samples	22.80 \pm 0.24	7.60 \pm 0.12	23.61 \pm 0.65	6.42 \pm 0.15	68.74 \pm 0.49	25.09 \pm 0.29	69.31 \pm 1.10	14.80 \pm 0.36	288.59 \pm 2.09	172.27 \pm 2.44
64 samples	21.80 \pm 0.24	7.46 \pm 0.11	24.32 \pm 0.95	6.36 \pm 0.18	67.23 \pm 0.37	24.77 \pm 0.22	67.38 \pm 1.06	14.41 \pm 0.34	281.63 \pm 1.90	160.00 \pm 2.21
128 samples	21.88 \pm 0.24	7.59 \pm 0.12	23.85 \pm 0.84	6.46 \pm 0.18	67.68 \pm 0.30	25.19 \pm 0.20	64.82 \pm 1.17	13.61 \pm 0.37	280.94 \pm 1.77	156.48 \pm 2.15
256 samples	21.83 \pm 0.26	7.55 \pm 0.14	22.27 \pm 0.74	6.09 \pm 0.18	67.53 \pm 0.32	25.19 \pm 0.21	65.53 \pm 1.07	13.84 \pm 0.35	276.74 \pm 1.90	151.73 \pm 2.51
512 samples	22.26 \pm 0.25	7.81 \pm 0.13	22.63 \pm 0.74	6.05 \pm 0.15	66.34 \pm 0.31	24.48 \pm 0.20	65.12 \pm 1.10	13.58 \pm 0.35	281.25 \pm 1.80	158.05 \pm 2.73

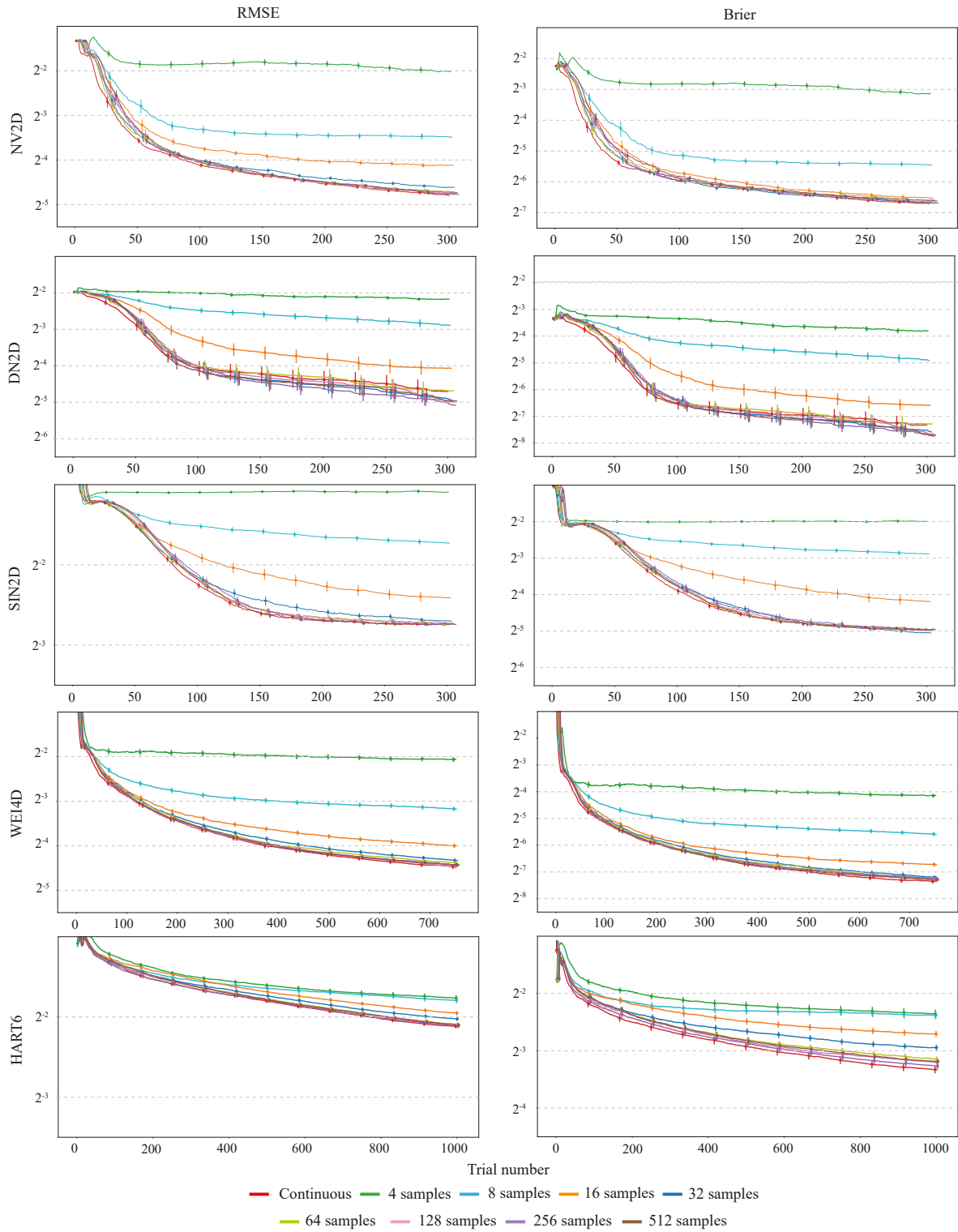


Figure 3: NEST RMSE errors for NV2D, DN2D, SIN2D, WEI4D, and HART6 with different numbers of discrete samples. Using between 4 and 16 samples per dimension is not enough to get a performance that is comparable to the continuous version, but using 32 or more samples typically is sufficient.

Method	NV2D detection		NV2D discrimination		ON2D detection		ON2D discrimination	
	AUC _{RMSE}	AUC _{Brier}	AUC _{RMSE}	AUC _{Brier}	AUC _{RMSE}	AUC _{Brier}	AUC _{RMSE}	AUC _{Brier}
NEST (ours)	22.69 ± 0.30	6.03 ± 0.15	16.78 ± 0.17	8.44 ± 0.16	13.94 ± 0.18	3.70 ± 0.08	16.85 ± 0.59	5.37 ± 0.36
QUEST+	N/A	N/A	N/A	N/A	N/A	N/A	N/A	N/A
BALD RBF	28.30 ± 0.18	11.27 ± 0.14	18.27 ± 0.21	10.63 ± 0.17	23.84 ± 0.15	6.31 ± 0.09	25.07 ± 0.31	5.48 ± 0.18
BALD mon.-RBF	27.78 ± 0.19	13.08 ± 0.17	16.72 ± 0.25	9.40 ± 0.20	22.89 ± 0.15	5.59 ± 0.08	25.00 ± 0.25	5.34 ± 0.15
BALD lin.-add.	35.78 ± 0.24	17.36 ± 0.25	20.12 ± 0.36	11.85 ± 0.37	29.23 ± 0.50	7.78 ± 0.16	31.71 ± 0.28	12.35 ± 0.37
BALV RBF	27.05 ± 0.17	10.45 ± 0.14	17.24 ± 0.21	8.84 ± 0.16	20.63 ± 0.13	5.41 ± 0.07	27.38 ± 0.34	7.24 ± 0.30
BALV mon.-RBF	26.05 ± 0.17	12.12 ± 0.15	18.47 ± 0.22	10.31 ± 0.21	18.89 ± 0.10	5.29 ± 0.05	25.82 ± 0.29	5.73 ± 0.16
BALV lin.-add.	40.70 ± 0.24	19.31 ± 0.28	18.18 ± 0.26	9.65 ± 0.29	29.40 ± 0.07	8.56 ± 0.07	32.34 ± 0.31	9.65 ± 0.36
LSE RBF	37.68 ± 0.23	8.35 ± 0.08	15.82 ± 0.21	7.16 ± 0.16	27.93 ± 0.20	4.76 ± 0.04	29.95 ± 0.47	3.81 ± 0.20
LSE mon.-RBF	40.84 ± 0.22	8.33 ± 0.09	16.20 ± 0.22	7.87 ± 0.16	27.90 ± 0.21	4.32 ± 0.04	28.53 ± 0.61	3.37 ± 0.11
LSE lin.-add.	51.06 ± 0.19	7.45 ± 0.12	16.49 ± 0.29	6.88 ± 0.13	42.31 ± 0.13	4.76 ± 0.04	30.34 ± 0.34	4.90 ± 0.23
EAVC RBF	48.12 ± 0.34	11.23 ± 0.16	26.23 ± 0.54	13.81 ± 0.36	40.79 ± 0.46	8.33 ± 0.17	39.68 ± 1.60	17.65 ± 2.12
GlobalMI RBF	39.09 ± 0.31	11.85 ± 0.15	26.30 ± 0.59	15.23 ± 0.38	35.46 ± 0.27	7.88 ± 0.16	35.53 ± 1.61	16.01 ± 2.04
Method	DN2D detection		DN2D discrimination		MAX2D detection		MAX2D discrimination	
	AUC _{RMSE}	AUC _{Brier}	AUC _{RMSE}	AUC _{Brier}	AUC _{RMSE}	AUC _{Brier}	AUC _{RMSE}	AUC _{Brier}
NEST (ours)	48.18 ± 0.40	25.71 ± 0.30	41.37 ± 0.61	43.88 ± 1.09	16.42 ± 0.16	4.22 ± 0.06	20.81 ± 0.78	14.56 ± 0.87
QUEST+	N/A	N/A	N/A	N/A	7.19 ± 0.12	N/A	5.74 ± 0.11	N/A
BALD RBF	63.52 ± 1.40	26.10 ± 0.61	52.71 ± 0.47	49.73 ± 0.90	29.96 ± 0.10	8.65 ± 0.12	32.54 ± 0.09	10.34 ± 0.11
BALD mon.-RBF	61.38 ± 0.62	27.60 ± 0.39	42.36 ± 0.40	62.65 ± 0.81	32.92 ± 0.12	10.99 ± 0.13	32.55 ± 0.09	8.40 ± 0.07
BALD lin.-add.	103.45 ± 0.85	102.52 ± 1.75	69.99 ± 0.38	88.79 ± 0.73	28.18 ± 0.37	11.03 ± 0.28	50.09 ± 0.13	16.60 ± 0.28
BALV RBF	70.54 ± 1.50	31.14 ± 0.83	57.58 ± 0.63	53.61 ± 0.88	25.39 ± 0.13	8.09 ± 0.09	29.68 ± 0.09	9.56 ± 0.09
BALV mon.-RBF	63.10 ± 0.91	32.82 ± 0.65	57.93 ± 0.58	58.65 ± 1.01	34.51 ± 0.08	10.08 ± 0.09	27.54 ± 0.10	8.01 ± 0.07
BALV lin.-add.	150.03 ± 0.86	101.67 ± 1.02	73.53 ± 0.48	103.30 ± 0.84	52.37 ± 0.12	24.05 ± 0.20	52.64 ± 0.09	21.48 ± 0.15
LSE RBF	111.15 ± 1.40	44.08 ± 0.64	63.36 ± 0.48	58.34 ± 0.84	31.18 ± 0.40	6.21 ± 0.07	41.63 ± 0.18	5.61 ± 0.06
LSE mon.-RBF	94.03 ± 2.02	40.93 ± 0.99	62.86 ± 0.63	60.44 ± 1.15	32.44 ± 0.23	5.99 ± 0.08	44.41 ± 0.12	5.17 ± 0.06
LSE lin.-add.	130.79 ± 0.76	102.52 ± 0.60	76.47 ± 0.59	99.83 ± 0.67	65.77 ± 0.25	8.13 ± 0.15	75.64 ± 0.16	8.14 ± 0.06
EAVC RBF	78.82 ± 0.62	71.41 ± 1.38	39.71 ± 0.50	64.25 ± 0.76	30.38 ± 0.52	7.37 ± 0.12	51.49 ± 0.33	9.81 ± 0.12
GlobalMI RBF	127.67 ± 0.39	58.00 ± 0.96	75.53 ± 0.38	94.32 ± 1.31	23.64 ± 0.48	6.45 ± 0.13	43.09 ± 0.30	7.85 ± 0.11
Method	SIN2D detection		SIN2D discrimination		HART6 detection		HART6 discrimination	
	AUC _{RMSE}	AUC _{Brier}	AUC _{RMSE}	AUC _{Brier}	AUC _{RMSE}	AUC _{Brier}	AUC _{RMSE}	AUC _{Brier}
NEST (ours)	66.85 ± 0.32	25.01 ± 0.24	53.40 ± 0.76	53.35 ± 1.24	271.15 ± 2.00	158.80 ± 2.87	156.26 ± 0.69	169.79 ± 1.42
QUEST+	57.73 ± 1.01	N/A	28.59 ± 0.36	N/A	N/A	N/A	N/A	N/A
BALD RBF	119.34 ± 0.42	71.95 ± 0.34	66.30 ± 0.35	69.31 ± 0.42	287.09 ± 1.13	307.12 ± 5.16	167.50 ± 1.17	200.30 ± 2.35
BALD mon.-RBF	116.95 ± 0.52	68.60 ± 0.38	63.52 ± 0.26	68.75 ± 0.36	288.47 ± 3.25	307.05 ± 8.81	170.07 ± 2.67	195.39 ± 4.35
BALD lin.-add.	127.21 ± 0.39	78.15 ± 0.19	63.67 ± 0.30	73.44 ± 0.59	342.06 ± 0.80	360.31 ± 4.30	183.45 ± 1.07	262.51 ± 4.29
BALV RBF	121.79 ± 0.66	75.91 ± 0.52	66.20 ± 0.41	70.03 ± 0.69	287.18 ± 1.34	280.11 ± 4.08	177.26 ± 1.41	219.46 ± 2.88
BALV mon.-RBF	116.11 ± 0.52	67.59 ± 0.41	63.74 ± 0.36	66.79 ± 0.57	284.36 ± 1.74	281.93 ± 8.21	171.89 ± 1.84	205.22 ± 3.91
BALV lin.-add.	120.45 ± 0.30	78.22 ± 0.24	64.00 ± 0.39	69.58 ± 0.82	329.77 ± 1.21	347.69 ± 4.03	185.03 ± 0.95	267.77 ± 3.06
LSE RBF	116.62 ± 0.52	66.99 ± 0.51	74.29 ± 0.79	72.85 ± 0.57	342.44 ± 1.37	256.03 ± 4.48	173.81 ± 1.80	198.32 ± 3.45
LSE mon.-RBF	117.87 ± 0.49	67.58 ± 0.49	69.51 ± 0.90	62.58 ± 0.33	335.37 ± 2.36	266.34 ± 19.77	178.24 ± 6.70	195.70 ± 13.56
LSE lin.-add.	116.31 ± 0.20	73.10 ± 0.33	65.91 ± 0.75	66.29 ± 0.36	340.71 ± 1.46	327.82 ± 6.36	178.88 ± 1.53	232.13 ± 3.56
EAVC RBF	125.08 ± 0.49	83.17 ± 0.68	67.04 ± 0.60	72.55 ± 0.85	333.23 ± 0.81	216.01 ± 3.21	191.01 ± 2.68	195.51 ± 1.64
GlobalMI RBF	116.67 ± 0.31	66.53 ± 0.30	63.95 ± 0.34	71.26 ± 0.33	311.79 ± 0.51	253.46 ± 4.49	168.42 ± 1.26	200.23 ± 2.58
Method	PS8D detection		PS8D discrimination					
	AUC _{RMSE}	AUC _{Brier}	AUC _{RMSE}	AUC _{Brier}				
NEST (ours)	370.68 ± 0.87	204.16 ± 1.01	215.94 ± 0.51	272.73 ± 1.23				
QUEST+	N/A	N/A	N/A	N/A				
BALD RBF	375.09 ± 2.16	290.86 ± 2.34	215.40 ± 1.28	278.04 ± 4.13				
BALD mon.-RBF	401.96 ± 1.95	313.53 ± 1.86	220.64 ± 1.70	292.94 ± 4.99				
BALD lin.-add.	394.19 ± 1.01	282.32 ± 1.32	215.85 ± 0.90	275.89 ± 2.43				
BALV RBF	367.19 ± 1.97	282.28 ± 2.00	222.59 ± 1.43	291.17 ± 3.94				
BALV mon.-RBF	395.95 ± 1.56	307.94 ± 2.14	227.02 ± 2.01	304.46 ± 4.70				
BALV lin.-add.	395.71 ± 1.32	285.70 ± 1.44	224.10 ± 1.46	295.52 ± 3.65				
LSE RBF	405.42 ± 2.54	244.03 ± 3.38	229.19 ± 1.62	296.55 ± 3.89				
LSE mon.-RBF	407.75 ± 3.50	242.43 ± 4.99	233.93 ± 2.08	304.42 ± 4.59				
LSE lin.-add.	379.24 ± 1.23	202.10 ± 1.81	208.69 ± 1.48	233.22 ± 3.04				
EAVC RBF	328.22 ± 0.49	183.26 ± 0.71	187.66 ± 0.57	197.17 ± 1.33				
GlobalMI RBF	332.21 ± 0.56	204.72 ± 0.93	192.67 ± 0.60	211.61 ± 1.49				

Table 4: The mean AUC ± standard error of the RMSE and Brier metrics for the NV2D, ON2D, DN2D, MAX2D, SIN2D, HART6, and PS8D detection and discrimination functions. The best method and methods that are statistically similar ($p \geq 0.05$, Games-Howell test) to it are shown in bold typeface for each metric.

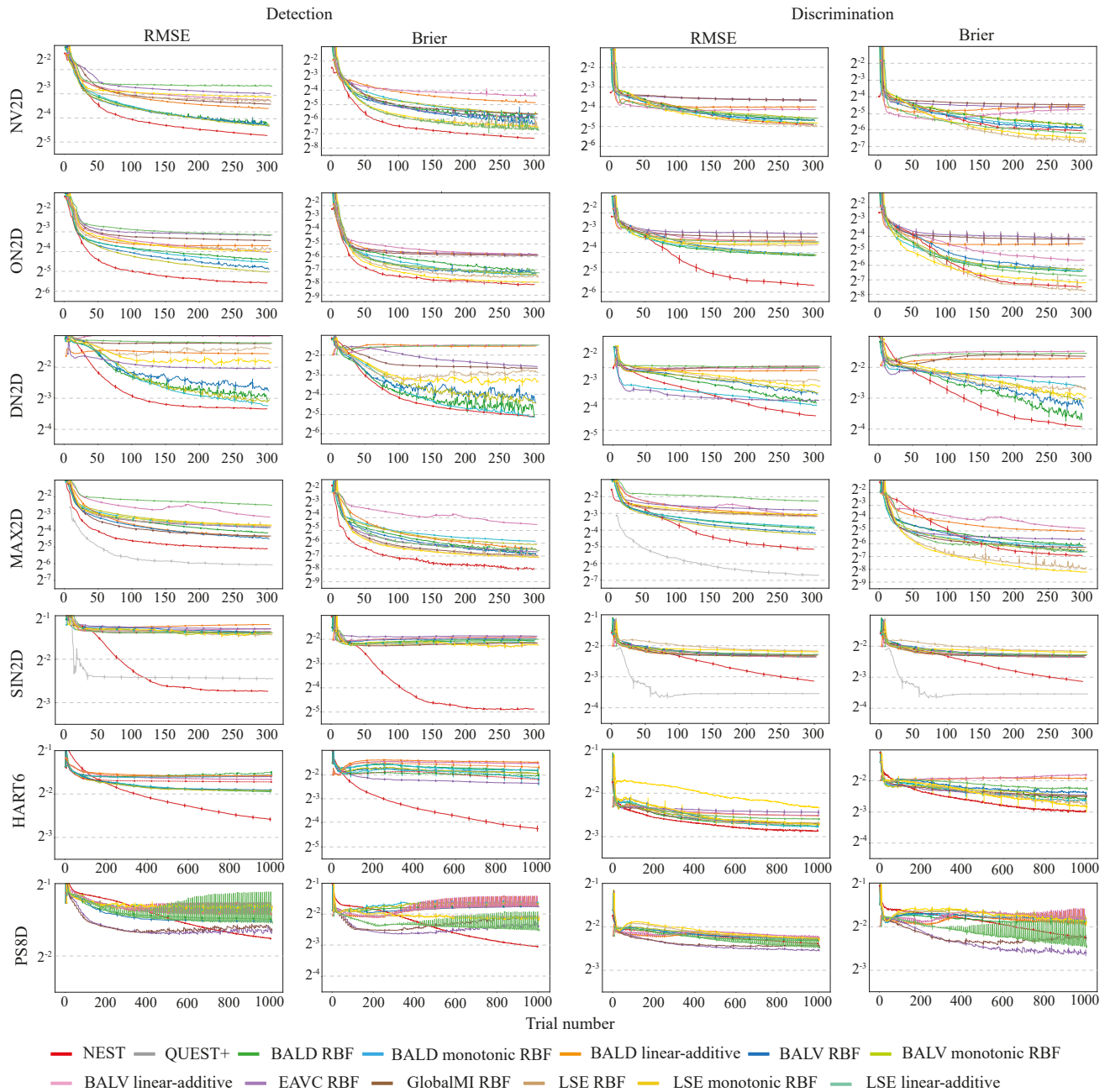


Figure 4: Simulation results for all test functions except the Weibull functions. NEST performs equally well or better in the most test cases. As mentioned in the main paper, GlobalMI and EAVC methods have a fast decrease in the error metrics at the beginning of the experiment for the PS8D function but eventually NEST achieves lower error scores. This is observable in the last row of the plots.

Method	WEI1D detection		WEI1D discrimination		WEI2D detection		WEI2D discrimination	
	AUC _{RMSE}	AUC _{Brier}	AUC _{RMSE}	AUC _{Brier}	AUC _{RMSE}	AUC _{Brier}	AUC _{RMSE}	AUC _{Brier}
NEST (ours)	10.17 ± 0.18	2.68 ± 0.07	10.19 ± 0.46	5.71 ± 0.32	15.76 ± 0.20	3.10 ± 0.08	23.21 ± 0.83	12.37 ± 0.67
QUEST+	4.99 ± 0.17	N/A	4.58 ± 0.16	N/A	16.35 ± 0.51	N/A	10.97 ± 0.32	N/A
BALD RBF	17.45 ± 0.13	5.36 ± 0.11	31.68 ± 0.44	10.75 ± 0.50	31.10 ± 0.26	12.18 ± 0.16	45.13 ± 0.48	18.73 ± 0.54
BALD mon.-RBF	29.61 ± 0.13	8.84 ± 0.10	39.89 ± 0.62	20.38 ± 0.68	26.01 ± 0.12	6.81 ± 0.08	40.35 ± 0.54	16.68 ± 0.53
BALD lin.-add.	173.89 ± 0.48	135.80 ± 0.38	79.48 ± 0.92	118.74 ± 4.35	68.04 ± 0.16	31.05 ± 0.34	50.78 ± 0.64	28.50 ± 0.91
BALV RBF	20.33 ± 0.44	7.15 ± 0.22	22.12 ± 0.38	8.94 ± 0.40	28.71 ± 0.10	8.76 ± 0.07	48.34 ± 0.61	26.98 ± 0.85
BALV mon.-RBF	23.56 ± 0.23	7.35 ± 0.13	48.01 ± 0.57	25.07 ± 0.90	24.87 ± 0.12	6.86 ± 0.09	50.19 ± 0.57	20.94 ± 0.84
BALV lin.-add.	177.48 ± 0.36	117.09 ± 1.12	64.05 ± 0.33	104.15 ± 2.68	57.36 ± 0.24	25.29 ± 0.21	50.78 ± 0.64	38.78 ± 1.22
LSE RBF	28.06 ± 0.26	2.74 ± 0.04	35.93 ± 1.43	7.98 ± 0.43	35.75 ± 0.26	5.70 ± 0.06	56.72 ± 1.24	9.91 ± 0.43
LSE mon.-RBF	38.19 ± 0.20	5.61 ± 0.08	57.19 ± 1.59	11.50 ± 0.53	31.16 ± 0.20	3.48 ± 0.04	49.73 ± 1.01	11.28 ± 0.45
LSE lin.-add.	155.03 ± 0.02	144.65 ± 3.05	70.46 ± 0.21	122.14 ± 2.01	74.33 ± 0.22	16.94 ± 0.14	59.87 ± 1.51	15.93 ± 0.72
EAVC RBF	28.17 ± 0.21	2.90 ± 0.04	30.15 ± 1.14	7.49 ± 0.46	31.93 ± 0.17	5.74 ± 0.05	46.34 ± 0.92	16.21 ± 0.66
GlobalMI RBF	13.93 ± 0.33	3.29 ± 0.07	23.63 ± 0.82	14.20 ± 0.65	26.42 ± 0.17	5.70 ± 0.06	43.69 ± 0.49	12.58 ± 0.41

Method	WEI3D detection		WEI3D discrimination		WEI4D detection		WEI4D discrimination	
	AUC _{RMSE}	AUC _{Brier}	AUC _{RMSE}	AUC _{Brier}	AUC _{RMSE}	AUC _{Brier}	AUC _{RMSE}	AUC _{Brier}
NEST (ours)	31.52 ± 0.61	4.62 ± 0.17	50.67 ± 0.78	14.38 ± 0.53	43.85 ± 0.80	8.14 ± 0.36	75.69 ± 1.13	20.20 ± 0.99
QUEST+	55.27 ± 1.82	N/A	34.35 ± 1.26	N/A	110.74 ± 3.82	N/A	82.76 ± 3.02	N/A
BALD RBF	104.44 ± 0.65	62.23 ± 0.75	77.34 ± 0.67	126.80 ± 1.01	77.91 ± 0.25	18.89 ± 0.17	102.88 ± 0.80	35.79 ± 0.62
BALD mon.-RBF	42.39 ± 0.19	8.59 ± 0.11	77.02 ± 0.91	25.79 ± 0.83	76.88 ± 0.32	23.73 ± 0.22	99.57 ± 1.59	33.55 ± 1.25
BALD lin.-add.	108.59 ± 0.51	44.66 ± 0.39	72.29 ± 0.51	34.00 ± 2.34	106.47 ± 0.60	23.77 ± 0.06	86.25 ± 0.86	28.84 ± 0.47
BALV RBF	122.76 ± 0.37	58.02 ± 0.15	74.63 ± 1.10	116.07 ± 1.92	100.33 ± 0.30	24.24 ± 0.27	105.09 ± 1.12	29.84 ± 0.81
BALV mon.-RBF	42.38 ± 0.24	8.43 ± 0.14	81.23 ± 1.37	32.23 ± 1.27	57.46 ± 0.63	10.46 ± 0.25	100.57 ± 1.79	23.71 ± 0.73
BALV lin.-add.	112.89 ± 0.31	59.06 ± 0.26	80.92 ± 0.73	45.40 ± 0.83	129.73 ± 0.71	39.18 ± 0.22	109.41 ± 1.73	23.26 ± 0.68
LSE RBF	87.72 ± 1.24	43.90 ± 0.40	64.50 ± 1.92	93.42 ± 2.70	73.82 ± 0.32	7.31 ± 0.06	121.59 ± 1.74	21.92 ± 0.34
LSE mon.-RBF	53.68 ± 0.36	7.48 ± 0.07	82.46 ± 2.21	14.88 ± 0.40	119.14 ± 3.57	27.15 ± 0.96	119.14 ± 3.57	19.85 ± 0.55
LSE lin.-add.	97.14 ± 0.35	18.44 ± 0.21	78.35 ± 1.30	28.27 ± 0.44	145.64 ± 2.58	42.47 ± 1.26	112.87 ± 1.43	34.57 ± 0.54
EAVC RBF	73.47 ± 0.47	14.76 ± 0.24	79.85 ± 1.19	13.89 ± 0.45	78.81 ± 0.52	10.61 ± 0.16	109.41 ± 1.73	23.64 ± 0.41
GlobalMI RBF	53.14 ± 0.30	11.66 ± 0.24	73.19 ± 1.25	12.86 ± 0.31	102.60 ± 0.41	22.31 ± 0.35	103.80 ± 1.83	26.15 ± 0.48

Table 5: The mean AUC ± standard error of the RMSE and Brier metrics for the WEI1D-4D functions. The best method and methods that are statistically similar ($p \geq 0.05$, Games-Howell test) to it are shown in bold typeface for each metric.

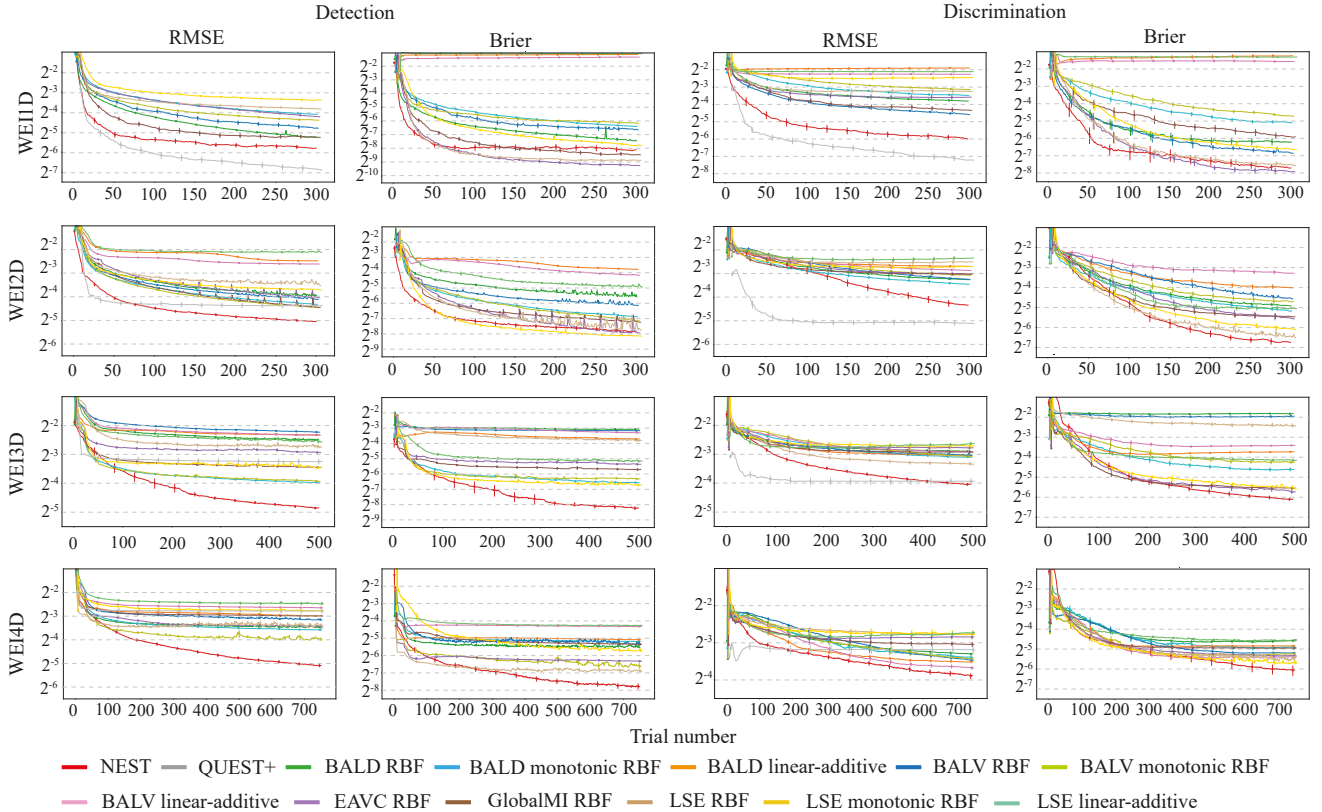


Figure 5: Simulation results for the Weibull test functions. NEST performs best in most test cases.

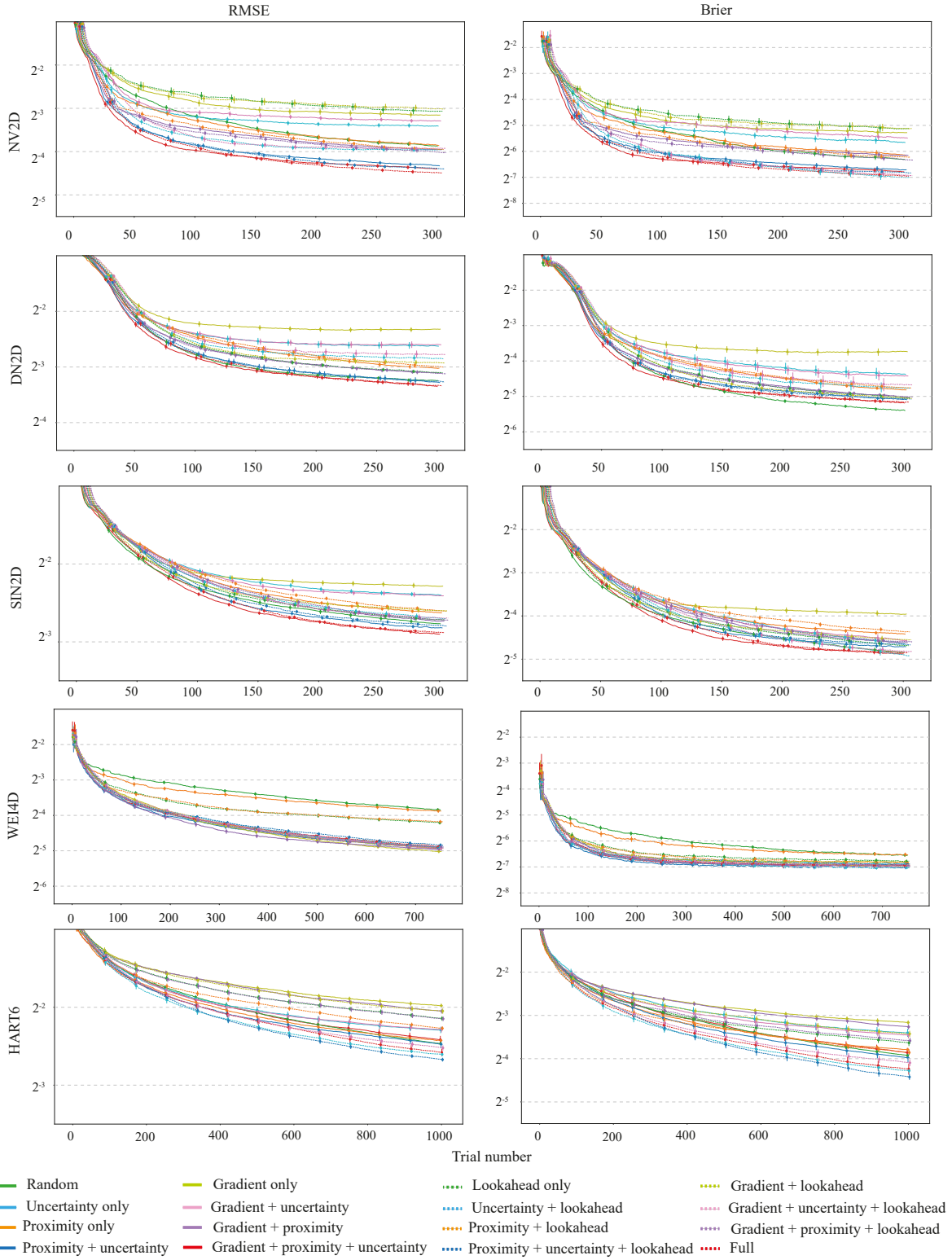


Figure 6: NEST ablation results for NV2D, DN2D, SIN2D, WEI4D, and HART6. We see that the different components are relevant for different functions and that the combined acquisition function always performs best or similarly to the other best options. The lookahead component has the most significant impact in the estimation of higher-dimensional functions such as the HART6 function.

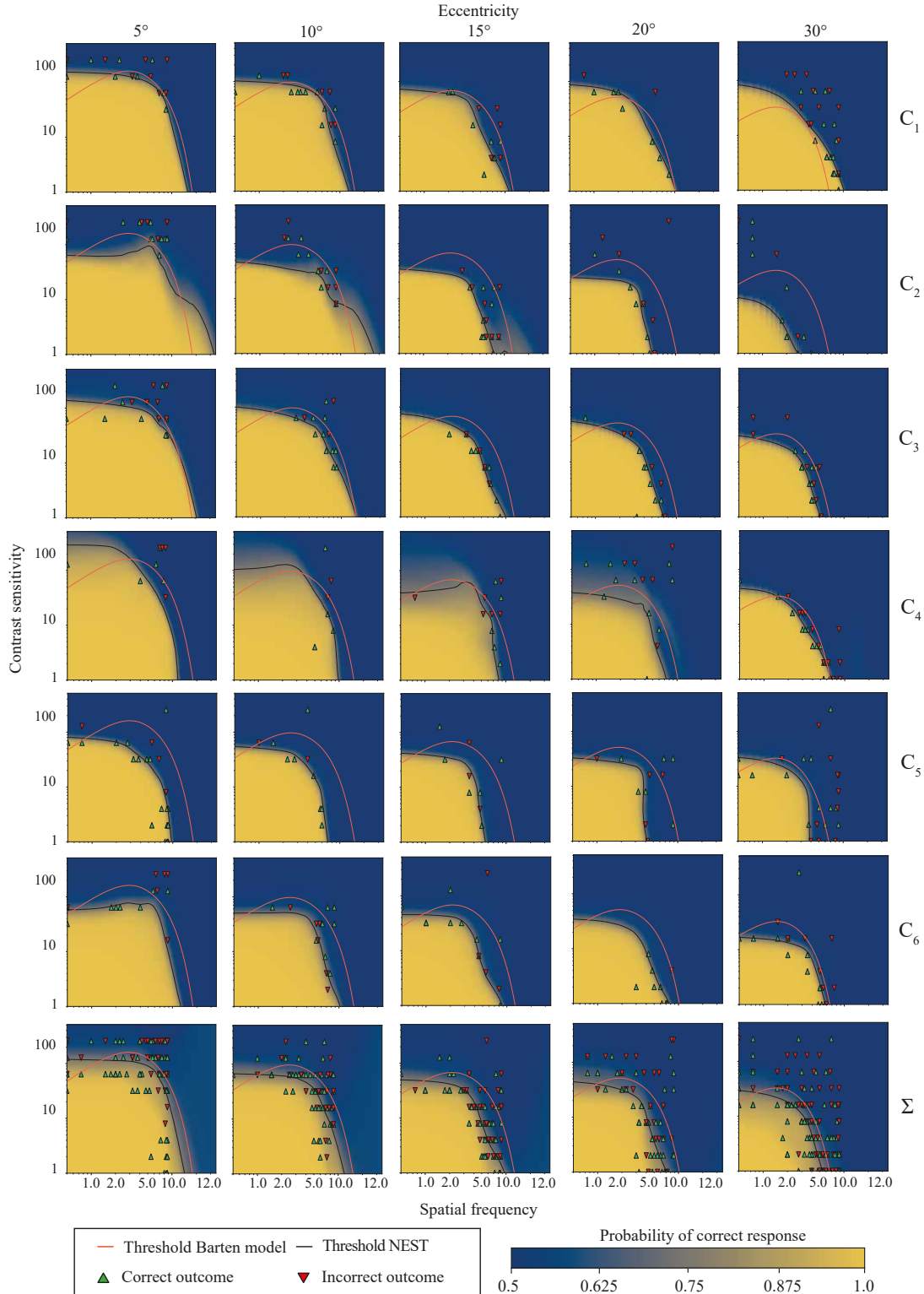


Figure 7: Results of the CSF experiment for multiple eccentricities. Each row shows the results for a different participant (labelled $C_1 - C_6$), and the bottom row (labelled Σ) shows the results when training a network on the combined data of the participants. The individual trial outcomes are shown as upward-pointing (correct) or downward-pointing (incorrect) triangles, and the detection thresholds of the theoretical model and the NEST method are shown as red and black lines, respectively. NEST learns a function that closely aligns with the fitted theoretical model.

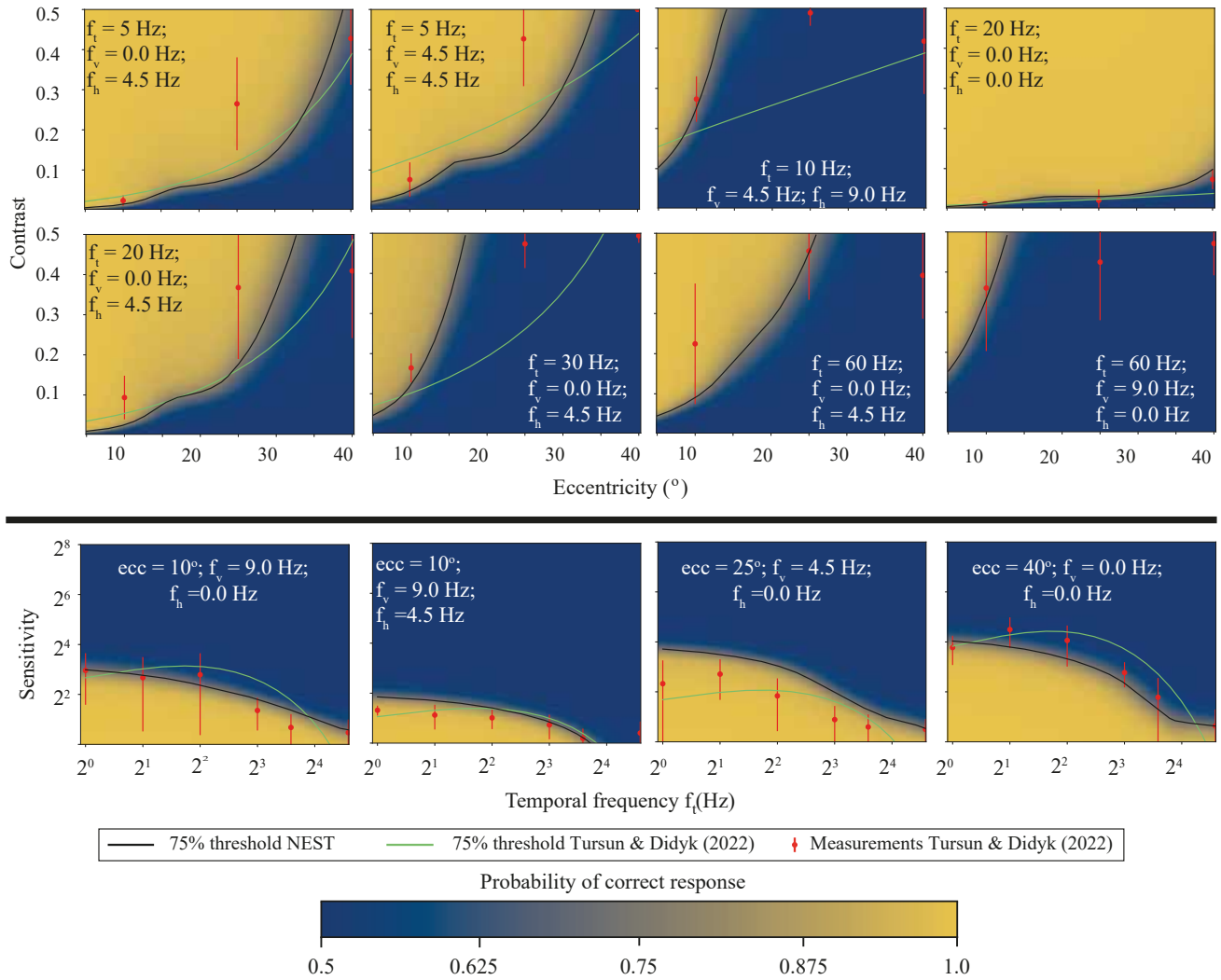


Figure 8: Results of the spatio-temporal experiment for participant P1.

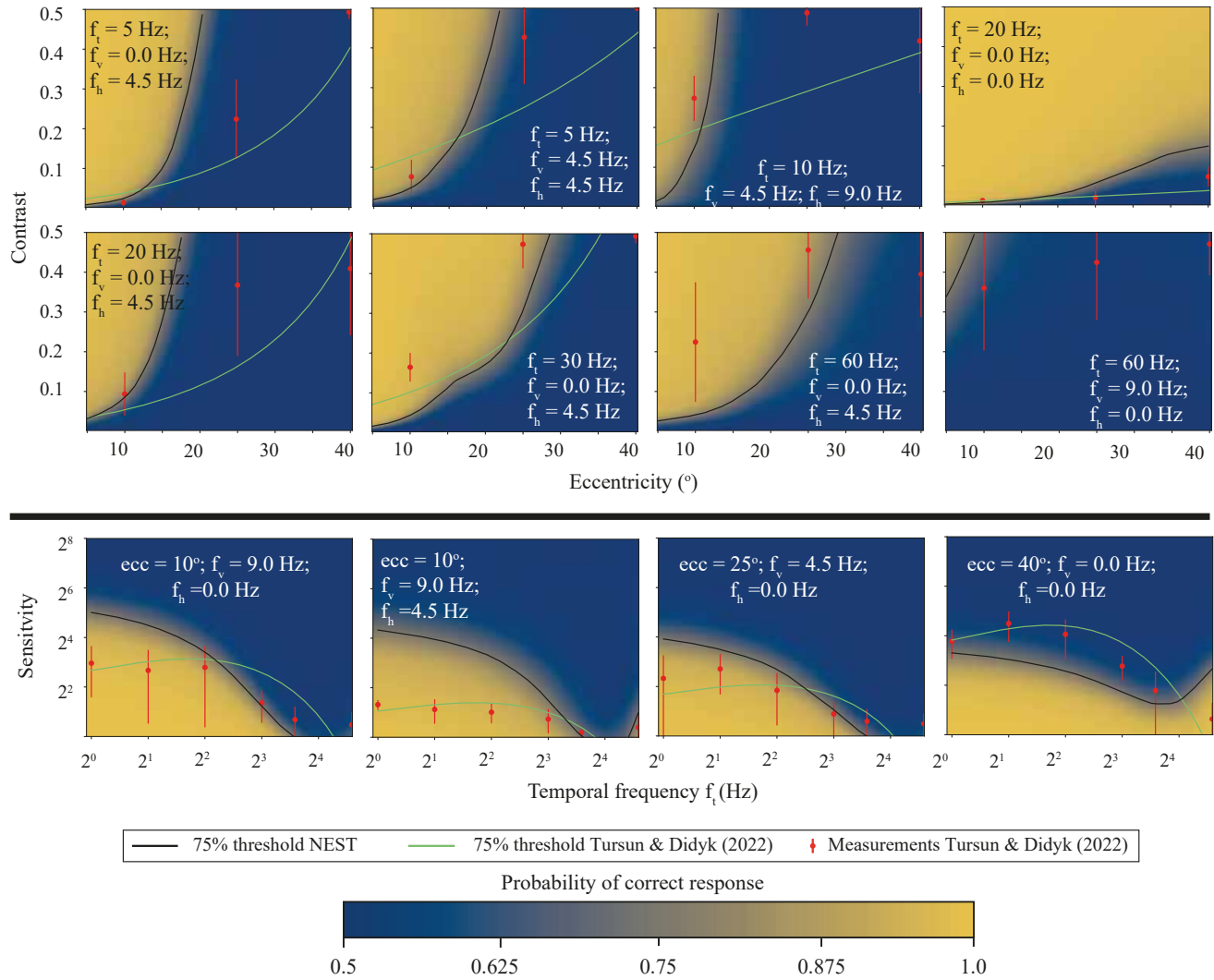


Figure 9: Results of the spatio-temporal experiment for participant P2.

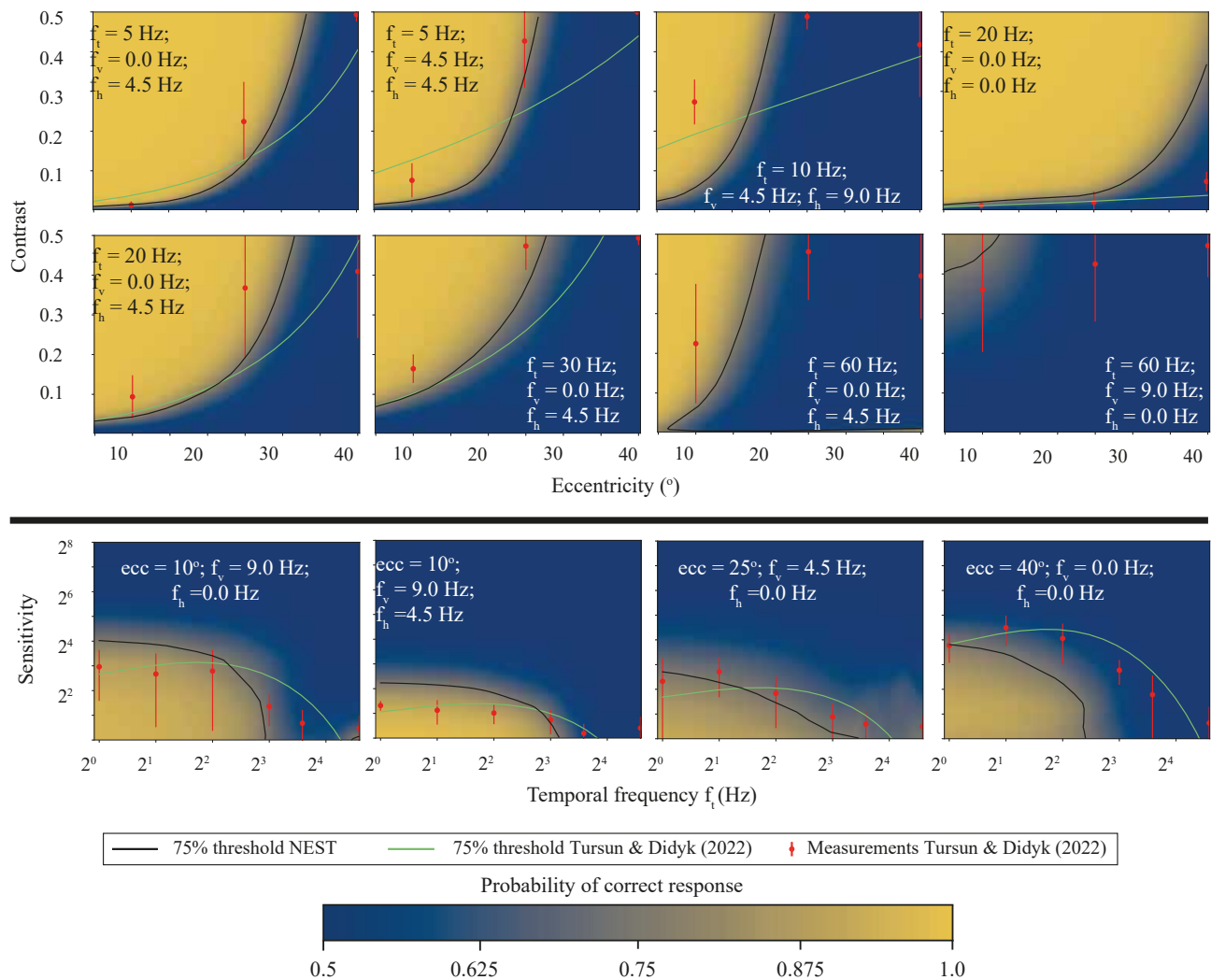
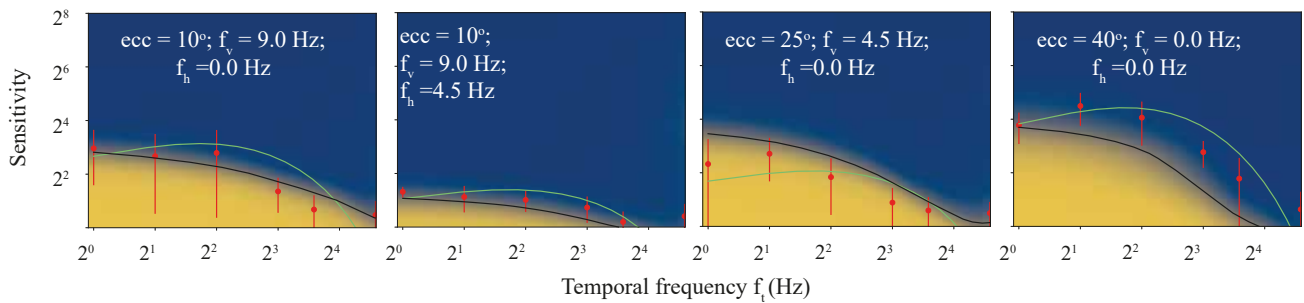
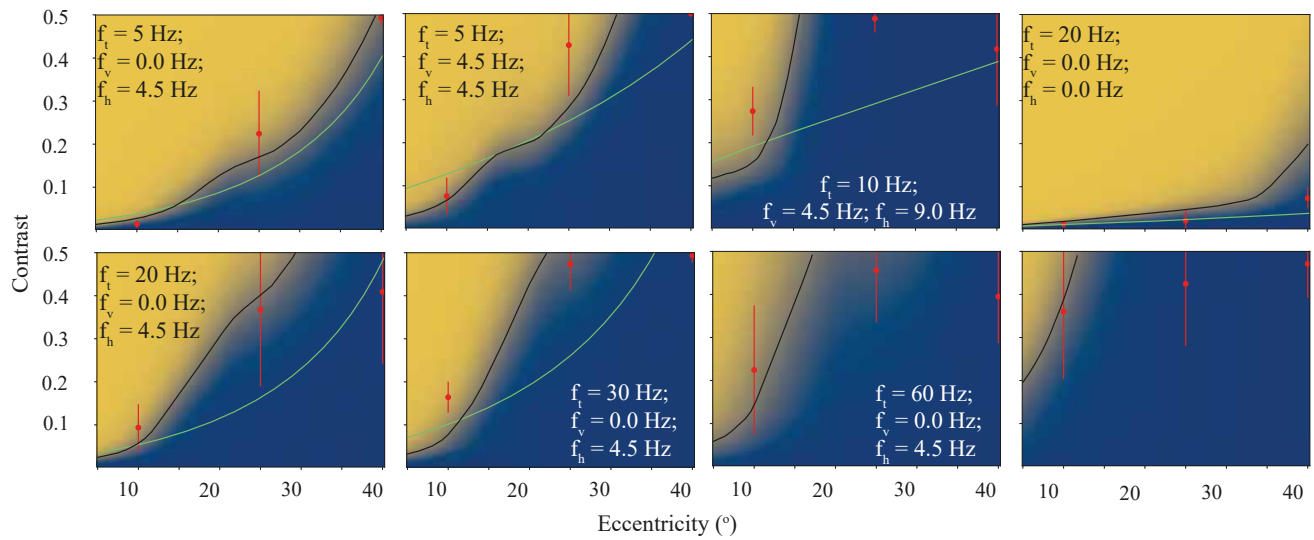


Figure 10: Results of the spatio-temporal experiment for participant P3.



75% threshold NEST
 75% threshold Tursun & Didyk (2022)
 Measurements Tursun & Didyk (2022)

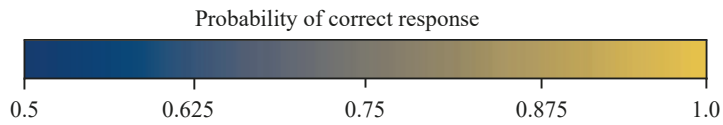


Figure 11: Results of the spatio-temporal experiment for participant P4.

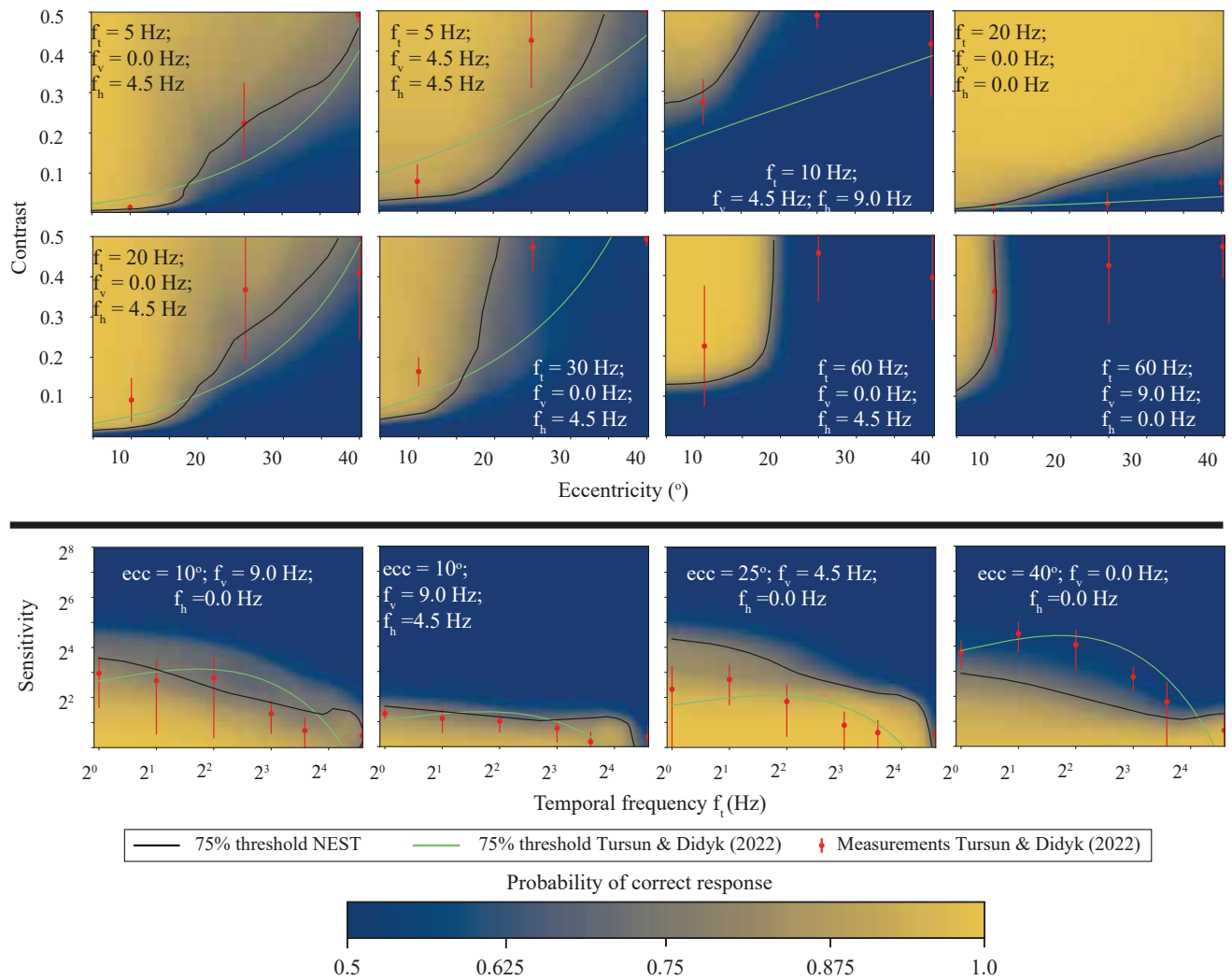


Figure 12: Results of the spatio-temporal experiment for participant P5.

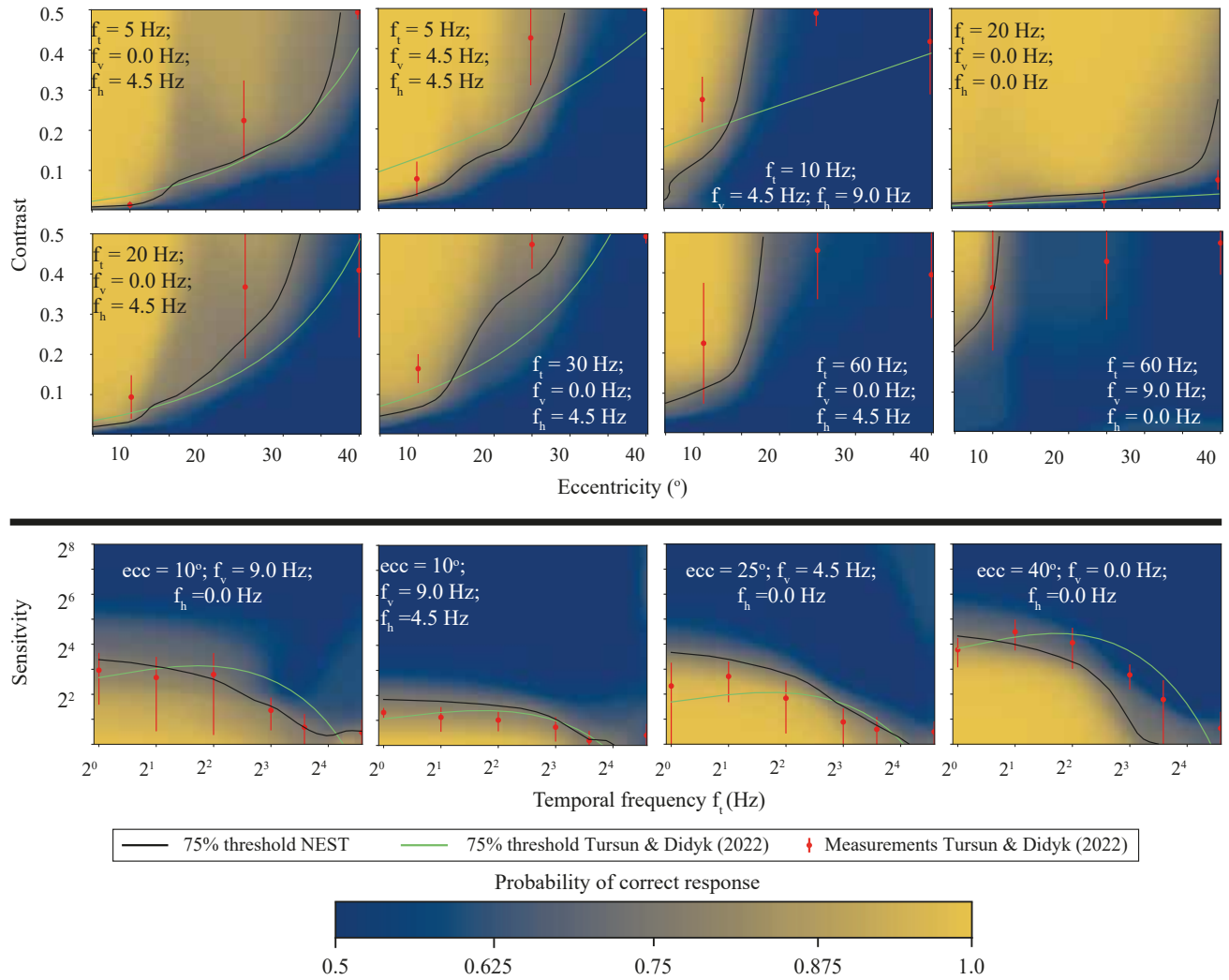


Figure 13: Combined results of the spatio-temporal experiment for all participants.